

Perturbative Field-Theoretical Analysis of Three-Species Cyclic Predator-Prey Models

Louie Hong Yao¹, Mohamed Swailem¹, Ulrich Dobramysl² & Uwe C. Täuber^{1,3}

¹ Department of Physics & Center for Soft Matter and Biological Physics, MC 0435, Robeson Hall, 850 West Campus Drive, Virginia Tech, Blacksburg, VA 24061, USA

² Peter Medawar Building for Pathogen Research, University of Oxford, Oxford OX1 3SY, United Kingdom

³ Faculty of Health Sciences, Virginia Tech, Blacksburg, VA 24061, USA

E-mail: hyao0731@vt.edu, mswailem@vt.edu, ulrich.dobramysl@gmail.com, tauber@vt.edu

16 March 2023

Abstract. We apply a perturbative Doi–Peliti field-theoretical analysis to the stochastic spatially extended symmetric Rock–Paper–Scissors (RPS) and May–Leonard (ML) models, in which three species compete cyclically. Compared to the two-species Lotka–Volterra predator-prey (LV) model, according to numerical simulations, these cyclical models appear to be less affected by intrinsic stochastic fluctuations. Indeed, we demonstrate that the qualitative features of the ML model are insensitive to intrinsic reaction noise. In contrast, and although not yet observed in numerical simulations, we find that the RPS model acquires significant fluctuation-induced renormalizations in the perturbative regime, similar to the LV model. We also study the formation of spatio-temporal structures in the framework of stability analysis and provide a clearcut explanation for the absence of spatial patterns in the RPS system, whereas the spontaneous emergence of spatio-temporal structures features prominently in the LV and the ML models.

Keywords: predator-prey model, cyclic competition, field-theoretical analysis, pattern formation, fluctuation-induced behavior

1. Introduction

Population dynamics has been and continues to be an extremely active field of research since about forty years [1, 2, 3, 4]. Steady progress in the development of mathematical and computational tools as well as the application of methods from statistical physics have allowed qualitative and quantitative insight into the behavior of interacting species. Various simplified models have been invoked to address prototypical situations in real ecosystems: The paradigmatic two-species Lotka–Volterra (LV) predator-prey model [5, 6] was originally introduced to study fish population oscillations in the Adriatic

sea, as well as to explain auto-catalytic chemical reaction cycles. The Rock-Paper-Scissors (RPS) model [4, 7, 8, 9, 10] addresses the case of three cyclically interacting species with a conserved total number of individuals, whereas the May–Leonard (ML) model [1, 11, 12, 13, 14, 15, 16] describes a more general, non-conserved situation. These models are obviously and necessarily rather simplified and lack many of the details of ecological neighborhoods. However, recent efforts aim at the realization and experimental implementation of such systems [17, 18, 19, 20, 21, 22]. Furthermore, it is reasonable to assume that simplified constructs such as the LV, ML, and RPS systems should be useful as elementary motifs and building blocks of models for more extended ecosystems. It is therefore imperative to investigate which of their features are qualitatively and/or quantitatively robust and remain important when multiple interacting species are coupled to environments with richer structures.

Traditionally, species dynamics in ecosystems are modelled via coupled non-linear ordinary differential equations. In the case of spatially extended systems, this approach is generalized by using partial differential equations that represent species dispersion through simple diffusion, i.e., coupled reaction-diffusion equations. However, this mean-field or mass action approach fails to take into account the inherent randomness and stochastic nature of the underlying processes stemming from fluctuations in the discrete number of individuals, and neglects spatio-temporal correlations. Yet fluctuations and correlations can lead to dramatically different behavior than predicted by mean-field theory [23]. For example, the classical LV mean-field rate equations predict neutral cycles and hence non-linear oscillations around a marginal fixed point, while stochastic computer simulations of this system yield decaying oscillations towards a (quasi-)stable state [24, 25, 26]. This stationary state exhibits large and erratic excursions triggered by fluctuations in the species concentrations in zero-dimensional [27] as well as spatially extended systems [28]. Spatially extended stochastic LV model variants also show intriguing spatial patterns and moving activity fronts [25, 29, 30]. Crucially, stochastic variants of the LV model exhibit a large susceptibility to randomness in the predator-prey interaction rates [31, 32].

Spatially extended cyclic models such as the RPS or ML systems are influenced by internal reaction noise and exhibit differences in species extinction times and resulting spiral pattern wavelengths compared to the mean-field approximation [9, 14, 33]. Although both models are cyclic in nature, they exhibit different sensitivity to stochastic fluctuations. The RPS model, a generalization of the LV model to three cyclically competing species, displays comparatively weak fluctuation renormalizations in the quasi-stable coexistence state and minimal modifications due to randomized reaction rates [10]. In contrast, the ML model features a stronger renormalization of the oscillation frequency in the unstable region where spiral structures form spontaneously, but appears to have an insignificant response to randomized reaction rates [13]. These observations from Monte Carlo simulations raise the intriguing question: Under what conditions will fluctuations significantly alter the system’s properties and cause marked deviations from simple mean-field predictions?

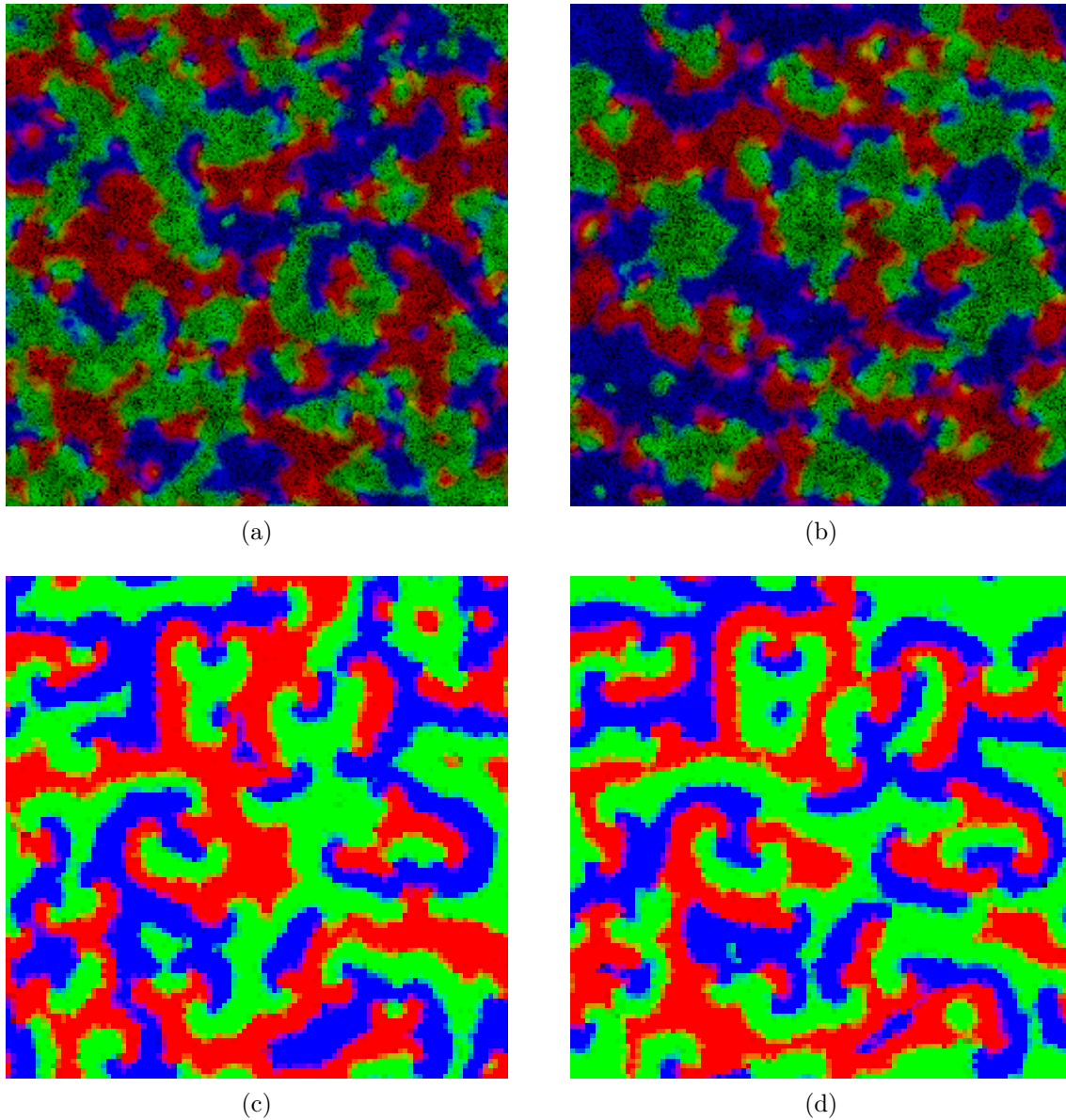


Figure 1. Snapshots of the spatial particle distribution in cyclic three-species RPS models for single stochastic simulation runs (system size 100×100 lattice sites): Each lattice pixel is assigned an RGB value such that each color value is proportional to the number of individuals of a specific species. A color value 0 represents the absence of the species corresponding to that assigned color; therefore, black pixels indicate empty sites. Top: RPS model with reaction rate parameter $\lambda' = 0.5$ at (a) $t = 300$ Monte Carlo Steps (MCS) and (b) $t = 400$ MCS; bottom: ML model with predation rate $\sigma' = 0.5$ and reproduction rate $\mu = 0.5$ at (c) $t = 300$ MCS and (d) $t = 400$ MCS, respectively. The red species predate on the blue species, the blue species on the green species, and the green species on the red species in both models.

To at least partially answer this question, a field-theoretical perturbation analysis was applied to the stochastic spatially extended LV model in Ref. [34]. To one-loop order, this semi-quantitative analysis confirms that i) the fluctuation-induced damping renders

the system unstable against spatio-temporal structures, and ii) fluctuations significantly renormalize the oscillation frequency in the two-species co-existence phases, especially below three dimensions. Aiming to better understand the fluctuations in spatially extended RPS [Fig. 1(a,b)] and ML models [Fig. 1(c,d)], we utilize a similar Doi–Peliti field theory representation for their associated stochastic reaction processes. To study the impact of intrinsic fluctuations on system parameters, a one-loop calculation is carried out, and a thorough comparison between the RPS, ML, and LV systems is conducted. In contrast to earlier observations in numerical simulations, the RPS model exhibits noticeable fluctuation-induced corrections in the perturbative regime, similar to the LV model. We believe that, as the dissipation becomes non-negligible in the non-perturbative regime, the associated infra-red (IR) divergence is regularized, and thus substantial renormalizations become effectively suppressed. We note that in all investigated systems, the field-theoretic loop expansion technically only applies to the stable regions with spatially homogeneous ground states. Our results demonstrate that, at least in the stable region, the dynamical features of the ML model conversely do not receive significant modifications from fluctuations. Based on these explicit calculation results, we also provide pertinent arguments that explain the absence of spontaneous spatio-temporal patterns in the RPS model with conserved total population number, as opposed to the ML model, which for sufficiently large system sizes develops spiral oscillatory patterns, as depicted in Fig. 1(c,d).

The paper is organized as follows: Detailed perturbative field-theoretical analyses for the cyclic and symmetric RPS and ML models are performed in sections II and III, respectively, where we establish the Doi–Peliti functionals for both models and state their corresponding generalized Langevin equations. Renormalized damping coefficients, oscillation frequencies, as well as diffusivities are calculated up to one-loop order in the perturbative fluctuation expansion. In section IV, a comprehensive comparison between the LV, RPS, and ML models is provided, and pertinent distinctions between these paradigmatic systems are highlighted. Specifically, we discuss the influence of fluctuations and the stability of spatio-temporal structures, and also briefly address the effect of quenched disorder in the reaction rates. We conclude with a brief summary and outlook. Finally, Appendix A presents a succinct review of the Doi–Peliti field theory approach and also provides a brief analysis of the asymmetric RPS model, demonstrating its effective two-species limit for strong asymmetry at the mean-field level. The remaining appendices list additional technical and computational details for the symmetric ML model.

2. Stochastic rock-paper-scissors (RPS) model

2.1. RPS model and mean-field rate equations

The RPS model consists of three particle species, subject to the cyclically coupled stochastic competition reactions



In this paper, we consider the cyclic-symmetric case, such that $\lambda'_1 = \lambda'_2 = \lambda'_3 = \lambda'$. In this limit, the system displays a discrete S_3 symmetry among the three species. A brief analysis of the general asymmetric case is presented in Appendix A. We note that every species interacts via a standard non-linear Lotka–Volterra predation reaction with the subsequent species in the cycle, consuming a “prey” particle and reproducing at the same instant. The total number of individuals is unchanged by all reactions, hence particle number conservation holds globally and locally (except for hops to neighboring lattice sites, see below).

We consider a model wherein particles from all three species perform random walks on a d -dimensional hyper-cubic lattice with L^d sites and lattice constant c . We do not restrict the number of particles per lattice site, hence we do not consider finite local carrying capacities here (the total number of particles is fixed). The rate at which particles hop between sites is given by D/c^2 , where D denotes a macroscopic diffusion constant. The reactions (1) occur on-site, and only if two particles of differing species are present. Reaction products are put on the same lattice point as the reactants.

In the limit of large diffusivities (relative to the reaction rates λ') the system can be considered well-mixed. Hence, the RPS rules can be approximated by the three coupled mean-field rate equations for the homogenized species concentrations and with the volume reactivities $\lambda = c^{-d}\lambda'$:

$$\begin{aligned} \frac{da_1(t)}{dt} &= \lambda a_1(t)[a_2(t) - a_3(t)] , \\ \frac{da_2(t)}{dt} &= \lambda a_2(t)[a_3(t) - a_1(t)] , \\ \frac{da_3(t)}{dt} &= \lambda a_3(t)[a_1(t) - a_2(t)] . \end{aligned} \tag{2}$$

This system of ordinary differential equations yields non-linear oscillations around a neutral fixed line which is determined by the initial conditions. The fixed-line steady-state concentrations can be obtained by setting the time derivatives to zero, resulting in

$$a_i^\infty = \frac{\rho}{3} , \quad \forall i \in \{1, 2, 3\} , \tag{3}$$

with the conserved total population density $\rho = a_1 + a_2 + a_3 = \text{const}$, parameterizing the fixed line. Linearization about this three-species coexistence fixed point yields the stability matrix

$$S_{\text{RPS}} = \frac{\lambda\rho}{3} \begin{pmatrix} 0 & +1 & -1 \\ -1 & 0 & +1 \\ +1 & -1 & 0 \end{pmatrix}, \quad (4)$$

with eigenvalues $\{0, -i\omega_0, i\omega_0\}$. Since the non-zero eigenvalues are purely imaginary, the mean-field RPS system performs perpetual non-linear oscillations around the coexistence fixed point with frequency (in the linearized approximation) $\omega_0 = \rho\lambda/\sqrt{3}$.

2.2. Doi–Peliti field theory and generalized Langevin equations

The bulk part of the Doi–Peliti action for the stochastic spatially extended RPS model follows directly from the reactions (1) and reads ‡

$$\mathcal{A}^{\text{RPS}} = \sum_{i=1,2,3} \int dt d^d x \hat{a}_i (\partial_t - D\nabla^2) a_i + \lambda \sum_{i=1,2,3} \int dt d^d x \hat{a}_i (\hat{a}_{i+1} - \hat{a}_i) a_i a_{i+1}. \quad (5)$$

For convenience, here we drop all position and time indices (\vec{x}, t) on the fields and identify $a_4 = a_1$. The first term describes the random nearest-neighbor hopping of the particles in the system, while the second contribution originates from the nonlinear reactions (1). As the auxiliary field $\hat{a}_i(\vec{x}, t)$ corresponds to a projection dual state, with average $\langle \hat{a}_i(\vec{x}, t) \rangle = 1$, a Doi shift $\tilde{a}_i(\vec{x}, t) = \hat{a}_i(\vec{x}, t) - 1$ is conveniently applied to have the new field averaged to $\langle \tilde{a}_i(\vec{x}, t) \rangle = 0$. After the Doi shift and ignoring boundary terms, the action becomes

$$\mathcal{A}^{\text{RPS}} = \sum_{i=1,2,3} \int dt d^d x \tilde{a}_i (\partial_t - D\nabla^2) a_i + \lambda \sum_{i=1,2,3} \int dt d^d x (\tilde{a}_i + 1) (\tilde{a}_{i+1} - \tilde{a}_i) a_i a_{i+1}. \quad (6)$$

This shifted action may now be viewed as a Janssen–De Dominicis response functional [37, 38] that represents the stochastic dynamics in terms of generalized Langevin equations. The \tilde{a}_i fields play the role of response fields and their coupling to the particle densities, shown in the terms that are second order in these fields, entails the presence of multiplicative noise terms. This comparison leads to the formulation of equivalent Langevin stochastic differential equations encoded in the action (6),

$$\partial_t a_i = D\nabla^2 a_i + \lambda a_i (a_{i+1} - a_{i-1}) + \zeta_i, \quad (7)$$

where $\zeta_i(\vec{x}, t)$ are the components of multiplicative noise in the system with vanishing means and correlations

$$\langle \zeta_i(\vec{x}_1, t_1) \zeta_j(\vec{x}_2, t_2) \rangle = 2Z_{ij} \delta^{(d)}(\vec{x}_1 - \vec{x}_2) \delta(t_1 - t_2), \quad (8)$$

‡ A brief introduction of the Doi–Peliti field theory representation is presented in Appendix A. We refer interested readers to Refs. [35, 36] for more details.

with the noise correlation matrix

$$Z = \lambda \begin{pmatrix} a_1 a_2 & -\frac{1}{2} a_1 a_2 & -\frac{1}{2} a_1 a_3 \\ -\frac{1}{2} a_1 a_2 & a_2 a_3 & -\frac{1}{2} a_2 a_3 \\ -\frac{1}{2} a_1 a_3 & -\frac{1}{2} a_2 a_3 & a_1 a_3 \end{pmatrix}. \quad (9)$$

Note that the noise auto-correlations Z_{ii} are always determined by the concentration of the predator species A_i and its respective prey A_{i+1} , and the scale is set by the predation rate λ . Hence the noise directly associated with a given species is solely determined by its role as predator.

2.3. Particle number conservation and Noether's theorem

Before we proceed with the perturbation theory analysis, we quickly comment on the conserved Noether current associated with the total particle number preservation in the stochastic reaction processes (1). This conservation law corresponds to a global $U(1)$ symmetry in the Doi–Peliti action (5) for the RPS model, namely it remains invariant under the $U(1)$ gauge transformation

$$\hat{a}'_i = e^{-i\theta} \hat{a}_i, \quad a'_i = e^{i\theta} a_i, \quad (10)$$

where θ is an arbitrary phase angle. The conservation law follows from the action (5) and the symmetry transformation (10) and assumes the usual form of a continuity equation

$$\partial_t j_0 + \nabla \cdot \vec{j} = 0, \quad (11)$$

with

$$j_0 = \sum_i \hat{a}_i a_i, \quad \vec{j} = -D \sum_i (\hat{a}_i \nabla a_i - a_i \nabla \hat{a}_i). \quad (12)$$

When choosing the Doi field $\hat{a}_i = 1$, a_i represents the density of particle species A_i and Eq. (12) turns into the diffusion equation for the conserved total particle number density,

$$\partial_t \sum_{i=1,2,3} a_i = D \nabla^2 \sum_{i=1,2,3} a_i. \quad (13)$$

We note that the symmetry (10) corresponds to the freedom of choosing the phases of the probability state a_i and its dual projected state \hat{a}_i .

2.4. Diagonalization of the harmonic action

To start, we transform the fields to describe the fluctuations around the stationary fixed-point species concentrations. To this end we employ the linear transformation

$$c_i(\vec{x}, t) = a_i(\vec{x}, t) - \frac{\rho}{3}, \quad \tilde{c}_i(\vec{x}, t) = \tilde{a}_i(\vec{x}, t), \quad (14)$$

which implies $\langle c_i \rangle = 0$. In the symmetric RPS model, there is both total particle number conservation and cyclic permutation symmetry among the three distinct species.

These two symmetries combined imply vanishing additive counterterms to the stationary concentrations due to fluctuations. The action for these new fluctuating fields now reads

$$\begin{aligned} \mathcal{A}^{\text{RPS}} = \int dt d^d x \sum_i \left[\tilde{c}_i (\partial_t - D\nabla^2) c_i - \frac{\lambda\rho^2}{3} \tilde{c}_i (\tilde{c}_i - \tilde{c}_{i+1}) - \frac{\lambda\rho}{3} \tilde{c}_i (\tilde{c}_{i+1} - \tilde{c}_{i+2}) \right. \\ \left. - \frac{\lambda\rho}{3} \tilde{c}_i^2 (c_i + c_{i+1}) + \frac{\lambda\rho}{3} \tilde{c}_i \tilde{c}_{i+1} (c_i + c_{i+1}) - \lambda \tilde{c}_i c_i (c_{i+1} - c_{i+1}) - \lambda \tilde{c}_i^2 c_i c_{i+1} + \lambda \tilde{c}_i \tilde{c}_{i+1} c_i c_{i+1} \right], \end{aligned} \quad (15)$$

where we again identify $c_4 = c_1$ and $c_5 = c_2$ for convenience. The quadratic part in the above action can be diagonalized by means of the following linear transformation

$$\begin{pmatrix} c_1 \\ c_2 \\ c_3 \end{pmatrix} = \frac{1}{\sqrt{3}} \begin{pmatrix} 1 & -\frac{1+i\sqrt{3}}{2} & -\frac{1-i\sqrt{3}}{2} \\ 1 & -\frac{1-i\sqrt{3}}{2} & -\frac{1+i\sqrt{3}}{2} \\ 1 & 1 & 1 \end{pmatrix} \begin{pmatrix} \phi_o \\ \phi_+ \\ \phi_- \end{pmatrix}, \quad (16)$$

and

$$\begin{pmatrix} \tilde{c}_1 \\ \tilde{c}_2 \\ \tilde{c}_3 \end{pmatrix} = \frac{1}{\sqrt{3}} \begin{pmatrix} 1 & -\frac{1-i\sqrt{3}}{2} & -\frac{1+i\sqrt{3}}{2} \\ 1 & -\frac{1+i\sqrt{3}}{2} & -\frac{1-i\sqrt{3}}{2} \\ 1 & 1 & 1 \end{pmatrix} \begin{pmatrix} \tilde{\phi}_o \\ \tilde{\phi}_+ \\ \tilde{\phi}_- \end{pmatrix}. \quad (17)$$

The resulting action becomes $\mathcal{A}^{\text{RPS}} = \mathcal{A}_0^{\text{RPS}} + \mathcal{A}_{\text{int}}^{\text{RPS}}$, with the Gaussian part

$$\mathcal{A}_0^{\text{RPS}} = \int dt d^d x \left[\tilde{\phi}_+ (\partial_t - D\nabla^2 + i\omega_0) \phi_+ + \tilde{\phi}_o (\partial_t - D\nabla^2) \phi_o + \tilde{\phi}_- (\partial_t - D\nabla^2 - i\omega_0) \phi_- \right], \quad (18)$$

and the nonlinear contributions (vertices)

$$\begin{aligned} \mathcal{A}_{\text{int}}^{\text{RPS}} = \int dt d^d x \left[-\lambda\rho^2 \tilde{\phi}_+ \tilde{\phi}_- + i\frac{\lambda\rho}{3} \tilde{\phi}_o (\tilde{\phi}_+ \phi_+ - \tilde{\phi}_- \phi_-) - \frac{2\lambda\rho}{\sqrt{3}} \tilde{\phi}_+ \tilde{\phi}_- \phi_o \right. \\ \left. - i\lambda (\tilde{\phi}_+ \phi_-^2 - \tilde{\phi}_- \phi_+^2 - \tilde{\phi}_+ \phi_+ \phi_o + \tilde{\phi}_- \phi_- \phi_o) \right. \\ \left. - i\frac{\lambda\rho}{6} \left[(1 - i\sqrt{3}) \tilde{\phi}_+^2 \phi_- - (1 + i\sqrt{3}) \tilde{\phi}_-^2 \phi_+ \right] + \text{four-point vertices} \right]. \end{aligned} \quad (19)$$

Here, $\omega_0 = \lambda\rho/\sqrt{3}$ denotes the zeroth-order oscillation frequency of the $\phi_{+/-}$ modes. $\mathcal{A}_0^{\text{RPS}}$ is the diagonalized harmonic part of the action, while $\mathcal{A}_{\text{int}}^{\text{RPS}}$ represents the ‘‘interaction’’ contributions for the perturbative expansion. We omit the explicit expressions for the four-point vertices as they will not contribute to the dispersion relations at one-loop order, which shall be clear in the calculation below. It is manifest that $\phi_o = (a_1 + a_2 + a_3 - \rho)/\sqrt{3}$ represents the fluctuation of the total particle number density. Due to the conservation law (13), the ϕ_o mode is purely diffusive, and its exact dispersion relation in the harmonic part of the action acquires no fluctuation corrections. The ϕ_+ and ϕ_- modes may be viewed as the left- and right-rotating waves in the system. At tree level, they are purely oscillating modes without dissipation, i.e., the real part of the mass term vanishes.

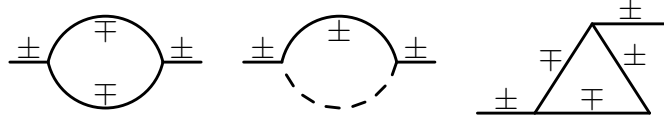


Figure 2. One-loop fluctuation contributions to the two-point vertex function $\Gamma_{\tilde{\phi}_{\pm}\phi_{\pm}}^{(1,1)}$ in RPS model. The solid lines represent the ϕ_{+} and ϕ_{-} modes, whereas the dashed lines represent the purely diffusive ϕ_o mode.

2.5. One-loop fluctuation corrections

We have applied a field-theoretical perturbation theory to one-loop order and calculated the renormalized diffusion constant D_r , damping constant γ_r , and oscillation frequency ω_r §. To all orders in the fluctuation expansion extending beyond the mean-field approximation, there should be no correction to the two-point vertex function $\Gamma_{\tilde{\phi}_o\phi_o}^{(1,1)}$ or propagator self-energy for the ϕ_o mode, whence it retains its tree-level purely diffusive dispersion relation as dictated by the conservation law. For the ϕ_{\pm} modes, the one-loop Feynman diagrams for the two-point vertex functions $\Gamma_{\tilde{\phi}_{\pm}\phi_{\pm}}^{(1,1)}$ are displayed in Fig. 2. The solid lines represent the ϕ_{+} and ϕ_{-} propagators, while the dashed lines indicate the diffusive mode ϕ_o . In our convention, time and hence momentum always flow from right to left in the Feynman diagrams. The analytic expression for the two-point vertex function $\Gamma_{\tilde{\phi}_{\pm}\phi_{\pm}}^{(1,1)}$ reads

$$\begin{aligned} \Gamma_{\tilde{\phi}_{\pm}\phi_{\pm}}^{(1,1)}(p, \omega) &= i\omega + Dp^2 + u_0 \pm i\omega_0 + \frac{\sqrt{3}\lambda\omega_0}{6D} \int_k I\left(\frac{u_0 \pm i\omega_0}{2D}\right) \\ &\quad - \frac{\sqrt{3}\lambda\omega_0}{6D} (1 \pm i\sqrt{3}) \int_k I\left(\frac{u_0 \mp i\omega_0}{D}\right) - \frac{\lambda\omega_0^2}{D^2} \int_k \frac{1}{k^2 + \frac{u_0}{D}} I\left(\frac{u_0 \mp i\omega_0}{D}\right), \end{aligned} \quad (20)$$

where \int_k is short-hand for the d -dimensional wavevector integral $\int d^d k / (2\pi)^d$, and the function I is defined as

$$I(m^2) = \frac{1}{k^2 + m^2 + \frac{i\omega + Dp^2}{2D} + p \cdot k}. \quad (21)$$

The damping constant u_0 in Eq. (20) is introduced to regularize the infrared (IR) singularities that emerge in later calculations. A nonzero renormalized u_r will be generated by the fluctuations, but it is of higher order in the perturbation expansion; thus, we need to take $u_0 \rightarrow 0$ at the end. This two-point function can also be expressed with the renormalized parameters as

$$\Gamma_{\tilde{\phi}_{\pm}\phi_{\pm}}^{(1,1)}(p, \omega) = Z_{\phi_{\pm}} (i\omega + D_r p^2 + u_r \pm i\omega_r), \quad (22)$$

where $Z_{\phi_{\pm}}$ absorbs all related wave function renormalizations (ultraviolet / UV divergences) in (20). The renormalized diffusivity D_r , damping u_r , and oscillation

§ For more details on the perturbation expansion and Feynman graph representations, we refer to Refs. [34, 35, 39].

frequency ω_r can be inferred accordingly from the explicit one-loop result (20) and (22). We obtain the following formal expressions for D_r , u_r , and ω_r ,

$$\begin{aligned}
D_r &= D + \frac{\sqrt{3}\lambda\omega_0}{6dD} \int_k \frac{k^2}{(k^2 \pm \frac{i\omega_0}{2D})^3} - \frac{\sqrt{3}\lambda\omega_0}{6dD} (1 \pm i\sqrt{3}) \int_k \frac{k^2}{(k^2 \mp \frac{i\omega_0}{D})^3} \\
&\quad - \frac{\lambda\omega_0^2}{dD^2} \int_k \frac{1}{(k^2 \mp \frac{i\omega_0}{D})^3}, \\
u_r \pm i\omega_r &= \pm i\omega_0 \left[1 - \frac{\lambda}{2D} \int_k \frac{1}{k^2 + \frac{u_0}{D}} \pm \frac{i\sqrt{3}\lambda}{6D} \int_k \left(\frac{1}{k^2 \mp \frac{i\omega_0}{D}} - \frac{1}{k^2 \pm \frac{i\omega_0}{2D}} \right) \right. \\
&\quad \left. + \frac{\sqrt{3}\lambda\omega_0}{12D^2} \int_k \frac{1}{(k^2 \pm \frac{i\omega_0}{2D})^2} - \frac{\sqrt{3}\lambda\omega_0}{12D^2} (1 \mp i\sqrt{3}) \int_k \frac{1}{(k^2 \pm \frac{i\omega_0}{2D})^2} \right].
\end{aligned} \tag{23}$$

Hence we indeed see that a non-zero damping u_r is generated at one-loop order from the fluctuations, in agreement with Monte Carlo simulation data [10]. The infra-red (IR) divergence at one-loop order that appears when in the renormalized oscillation frequency ω_r in low dimensions $d \leq 2$ is caused by the contribution of the massless ϕ_o mode as u_0 is set to zero. The infra-red (IR) divergence at one-loop order that appears in the renormalized oscillation frequency ω_r in low dimensions $d \leq 2$ is caused by the superposition of ϕ_+ and ϕ_- modes as u_0 is set to zero. Our analysis of the one-loop results shows that the ϕ_{\pm} modes are inherently massive, as they acquire non-zero damping u_r . Thus, the IR divergence can be resolved simply by maintaining a finite value for u_0 . For dimensions $d \geq 2$, there are also UV divergences present. Nevertheless, all systems of interest have a natural cutoff in the UV limit, which is defined by the lattice constant c . The renormalized variables in different physically accessible dimensions are presented below.

2.5.1. $d = 1$: In one dimension, the renormalized parameters are

$$\begin{aligned}
\text{Re}D_r &= D + \lambda\sqrt{\frac{D}{\omega_0}} \left(\frac{7\sqrt{2}}{64} + \frac{\sqrt{6}}{192} - \frac{\sqrt{3}}{48} \right), \\
\omega_r &= \omega_0 \left[1 - \frac{\lambda}{4D} \sqrt{\frac{D}{u_0}} - \frac{\lambda}{D} \sqrt{\frac{D}{\omega_0}} \left(\frac{\sqrt{3}}{8} + \frac{\sqrt{6}}{32} + \frac{\sqrt{2}}{32} \right) \right], \\
u_r &= \frac{\lambda\omega_0}{D} \sqrt{\frac{D}{\omega_0}} \left(\frac{\sqrt{3}}{8} - \frac{\sqrt{6}}{32} + \frac{\sqrt{2}}{32} \right);
\end{aligned} \tag{24}$$

some numerical results are depicted in Fig. 3. We observe that the renormalized frequency ω_r diverges when $u_0 \rightarrow 0$. This IR divergence indicates strong fluctuation corrections to the oscillation frequency in the perturbative regime where reaction rates are small, and $u_0 \rightarrow u_r \sim \lambda$ is of first order in the reactivity. However, numerical simulations are invariably performed outside this regime for the sake of computational efficiency, as large reaction rates are used to avoid long relaxation times. Thus, no strong

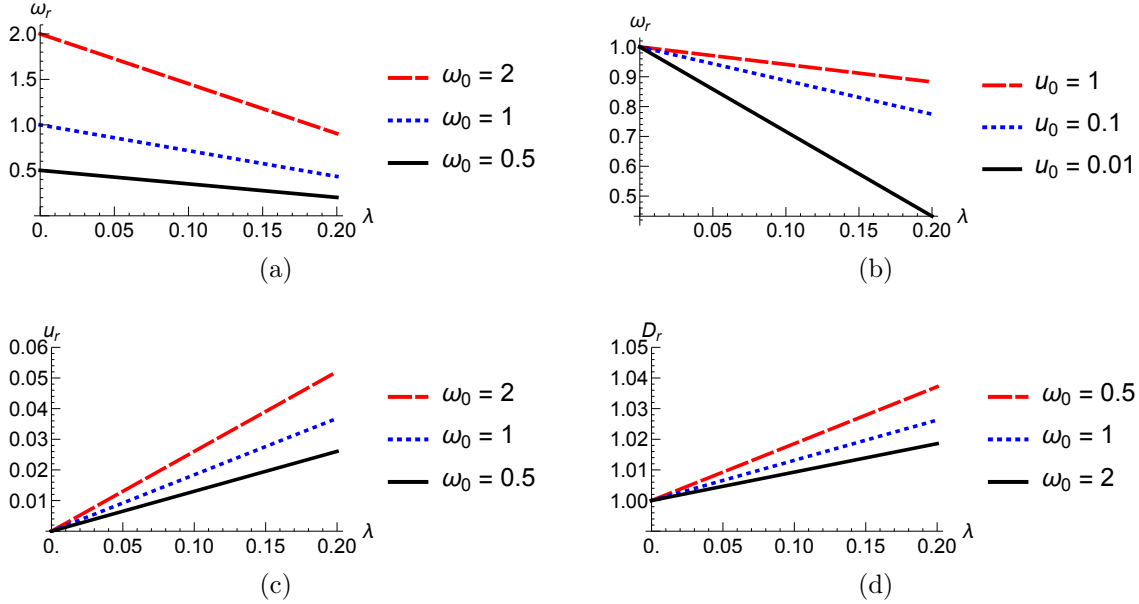


Figure 3. Renormalized parameters in one dimension ($d = 1$) in the RPS model: (a) Renormalized frequency ω_r as a function of the reactivity parameter λ , with $D = 1$, $u_0 = 0.01$, and for different bare frequencies ω_0 . (b) Renormalized frequency ω_r as a function of the parameter λ , with $\omega_0 = 1$, $D = 1$, and different bare damping coefficients u_0 . (c) Renormalized u_r as a function of the parameter λ with $D = 1$ and different bare frequencies ω_0 . (d) Renormalized diffusion constant D_r as a function of the parameter λ with $D = 1$ and different bare frequencies ω_0 .

fluctuation-induced renormalization have been encountered in the simulations. To one-loop order, $u_r > 0$, which indicates the stability of the system's spatially homogeneous ground state with respect to fluctuations.

2.5.2. $d = 2$: In two dimensions, the renormalized variables read

$$\begin{aligned}
 \text{Re}D_r &= D + \frac{3\lambda}{32\pi}, \\
 \omega_r &= \omega_0 \left[1 - \frac{\lambda}{8D\pi} \ln \left(\frac{D\Lambda^2}{u_0} \right) - \frac{\lambda}{D\pi} \left(\frac{1}{16} + \frac{\sqrt{3}\pi}{24} \right) \right], \\
 u_r &= \frac{\sqrt{3}\lambda\omega_0}{48D\pi} (3 + 2 \ln 2).
 \end{aligned} \tag{25}$$

Note that we have explicitly introduced the cutoff $\Lambda \sim \pi/c$ to regularize the UV divergence for the renormalized oscillation frequency. We plot ω_r and the damping parameter u_r in Fig. 4. The renormalized diffusion constant D_r only linearly depends on the parameter λ . As in the one-dimensional case, the oscillation frequency ω_r diverges as $u_0 \rightarrow 0$. We note that the damping constant u_r is also positive at $d = 2$.

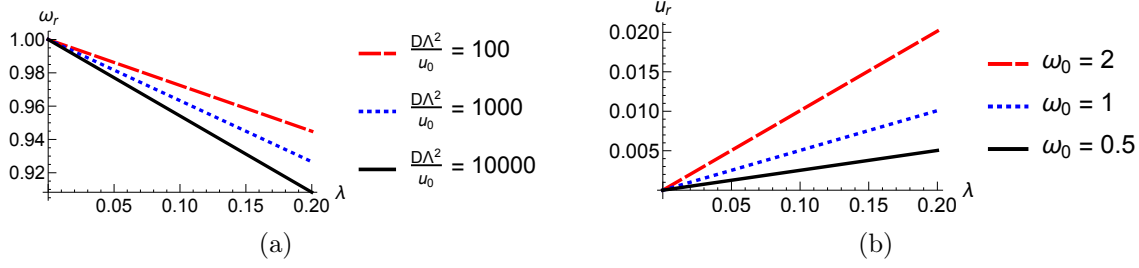


Figure 4. Renormalized parameters in two dimensions ($d = 2$) in the RPS model: (a) Renormalized frequency ω_r as a function of the reactivity parameter λ with $D = 1$ and different ratios DA^2/u_0 . (b) Renormalized damping u_r as a function of the parameter λ with $D = 1$ and different bare frequencies ω_0 .

2.5.3. $d = 3$: In three dimensions, we may safely set $u_0 = 0$ and the renormalized system parameters follow as

$$\begin{aligned} \text{Re}D_r &= D + \frac{\lambda}{\pi} \sqrt{\frac{\omega_0}{D}} \left(\frac{\sqrt{3}}{192} - \frac{\sqrt{6} - 5\sqrt{2}}{384} \right), \\ \omega_r &= \omega_0 \left[1 - \frac{\lambda}{D\pi} \sqrt{\frac{\omega_0}{D}} \left(\frac{\sqrt{3}}{96} + \frac{5\sqrt{6}}{192} + \frac{\sqrt{2}}{64} \right) \right], \\ u_r &= \frac{\lambda\omega_0}{D\pi} \sqrt{\frac{\omega_0}{D}} \left(-\frac{\sqrt{3}}{96} + \frac{5\sqrt{6}}{192} - \frac{\sqrt{2}}{64} \right). \end{aligned} \quad (26)$$

We notice that for $d > 2$ the IR divergences disappear and fluctuation effects become generally weak. u_r is also positive for $d = 3$, as displayed in Fig. 5.

We have found that in dimensions $d = 1, 2$, and 3 , the diffusivity D experiences an upward shift, indicating that fluctuations enhance the diffusion. Our results, depicted in Fig. 3, 4, and 5, show that as the reaction rate increases, the characteristic frequency ω_r shifts to smaller values, as the reactions drive the system towards a spatially more homogeneous distribution, leading to slower oscillations. The decline

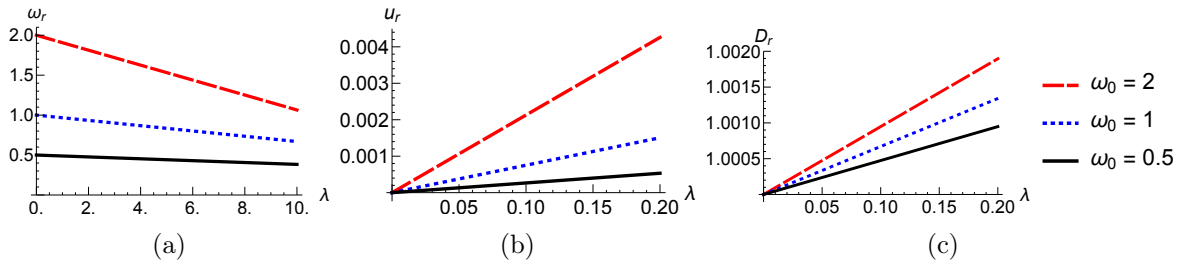


Figure 5. Renormalized parameters in three dimensions ($d = 3$) in the RPS model: (a) Renormalized frequency ω_r as a function of the reactivity parameter λ with $D = 1$ and different ratios DA^2/u_0 . (b) Renormalized damping u_r as a function of the parameter λ with $D = 1$ and different bare frequencies ω_0 . (c) Renormalized diffusion constant D_r as a function of the parameter λ with $D = 1$ and different bare frequencies ω_0 .

in the characteristic frequencies is in accordance with the numerical simulation data in Ref. [10]. In contrast with the LV model, Monte Carlo simulations of the RPS system do not appear to show strong renormalization effects [10], although both models feature a logarithmic divergence in two dimensions. The IR divergence in the RPS model appears as a consequence of the fact that the corrections are built using the Gaussian theory which has zero damping, precisely as in the LV model. The positive fluctuation-induced damping μ_r , in contrast to the possibly negative one in the LV model, indicates that the system remains stable against the spontaneous emergence of spatio-temporal structures.

3. Stochastic May–Leonard (ML) model

3.1. ML model and mean-field rate equations

The following discussion of the mean-field theory, Doi-Peliti action, and Langevin representation for the spatially extended stochastic ML model was laid out in detail in Ref. [16]. Here we summarize the pertinent points needed for our comparison with the RPS model and the computation of the fluctuation corrections to one-loop order. Following the conventions in Ref. [16], the reactions in the ML model read



where $i = 1, 2, 3$ denotes the three competing species, and we identify $B_4 = B_1$ as before. In contrast to the RPS system, the reactions in the ML model do not conserve the total particle number. The first two reactions implement predation and reproduction independently, while the third reaction implements “soft” site occupation constraint to effectively represent a finite carrying capacity. As in the RPS model, we consider a model wherein particles from all three species perform random walks on a d -dimensional hyper-cubic lattice with L^d sites and lattice constant c . In the large diffusivity limit, the dynamics is governed by the mean-field rate equations

$$\begin{aligned} \frac{db_1(t)}{dt} &= b_1(t) \left(-\sigma b_3(t) + \mu - \kappa b_1(t) \right), \\ \frac{db_2(t)}{dt} &= b_2(t) \left(-\sigma b_1(t) + \mu - \kappa b_2(t) \right), \\ \frac{db_3(t)}{dt} &= b_3(t) \left(-\sigma b_2(t) + \mu - \kappa b_3(t) \right), \end{aligned} \tag{28}$$

where $\sigma = c^d \sigma'$ and $\kappa = c^d \kappa'$ are the volume reaction rates. Instead of a fixed line defined by the initial condition, the ML system displays a unique fixed point at mean-field level. By setting the time derivatives to be 0, the steady-state concentrations are found to be

$$b_i^\infty = \frac{\mu}{\sigma + \kappa}, \quad \forall i \in \{1, 2, 3\}, \tag{29}$$

and the associated stability matrix reads

$$S_{\text{ML}} = -\frac{\mu}{\sigma + \kappa} \begin{pmatrix} \kappa & 0 & \sigma \\ \sigma & \kappa & 0 \\ 0 & \sigma & \kappa \end{pmatrix}. \quad (30)$$

Its eigenvalues at the coexistence fixed point are $\{-\mu, -\mu(2\kappa - \sigma \pm i\sqrt{3}\sigma)/2(\sigma + \kappa)\}$. The first eigenvalue $-\mu$ is always negative which implies the stability of the corresponding eigenmode, namely the exponential decay of the total particle number, see below. The imaginary part of the two complex conjugate eigenvalues, $\pm\sqrt{3}\mu\sigma/2(\sigma + \kappa)$, represents the frequency of temporal oscillations for the associate modes, whose amplitudes are either exponentially damped or growing. When $2\kappa > \sigma$, the real part of the complex eigenvalues is negative and the limit circles are stable. Otherwise, for $2\kappa < \sigma$, the limit circles are unstable and one observes the spontaneous formation of spiral structures in the system. In the vicinity of the Hopf bifurcation at $2\kappa = \sigma$, the time evolution of the two modes corresponding to the complex conjugate eigenvalues becomes much slower than the fast relaxing mode, which introduces a natural time scale separation. As a consequence of the critical slowing down near the Hopf bifurcation, the fast relaxing mode can be integrated out and the system is effectively governed by the complex time-dependent Ginzburg–Landau equation [16].

3.2. Doi–Peliti field theory and generalized Langevin equations

The Doi–Peliti action follows from the reactions of the ML model and reads

$$\begin{aligned} \mathcal{A}^{\text{ML}} = \sum_{i=1,2,3} \int dt d^d x \left[\hat{b}_i (\partial_t - D\nabla^2) b_i + \mu \hat{b}_i b_i (1 - \hat{b}_i) + \kappa \hat{b}_i b_i^2 (\hat{b}_i - 1) \right. \\ \left. + \sigma \hat{b}_i b_i b_{i+1} (\hat{b}_{i+1} - 1) \right]. \end{aligned} \quad (31)$$

This action does not obey the $U(1)$ global symmetry present in the RPS model; indeed, the total particle number is not conserved under the ML reactions (27). Following the Doi shift to the fluctuating auxiliary fields $\tilde{b}_i(\vec{x}, t) = \hat{b}_i(\vec{x}, t) - 1$, the action becomes

$$\begin{aligned} \mathcal{A}^{\text{ML}} = \sum_{i=1,2,3} \int dt d^d x \left[\tilde{b}_i (\partial_t - D\nabla^2 - \mu) b_i - \mu \tilde{b}_i^2 b_i + \kappa \tilde{b}_i b_i^2 (\tilde{b}_i + 1) \right. \\ \left. + \sigma \tilde{b}_{i+1} b_i b_{i+1} (\tilde{b}_i + 1) \right]. \end{aligned} \quad (32)$$

As in the RPS model above, we may now view this shifted action as a Janssen–De Dominicis functional which is equivalent to the corresponding generalized Langevin equations

$$\partial_t b_i = D\nabla^2 b_i + \mu b_i - \kappa b_i^2 - \sigma b_i b_{i+2} + \xi_i, \quad (33)$$

where $\xi_i(\vec{x}, t)$ represent the multiplicative noise components with correlators

$$\langle \xi_i(\vec{x}_1, t_1) \xi_j(\vec{x}_2, t_2) \rangle = 2\Xi_{ij} \delta^{(d)}(\vec{x}_1 - \vec{x}_2) \delta(t_1 - t_2), \quad (34)$$

with

$$\Xi = \begin{pmatrix} \mu b_1 - \kappa b_1^2 & -\frac{\sigma}{2} b_1 b_2 & -\frac{\sigma}{2} b_1 b_3 \\ -\frac{\sigma}{2} b_1 b_2 & \mu b_2 - \lambda b_2^2 & -\frac{\sigma}{2} b_2 b_3 \\ -\frac{\sigma}{2} b_1 b_3 & -\frac{\sigma}{2} b_2 b_3 & \mu b_3 - \lambda b_3^2 \end{pmatrix}. \quad (35)$$

3.3. Diagonalization of the harmonic action

Before diagonalizing the quadratic action, we first shift to fluctuating fields, $\tilde{d}_i(\vec{x}, t) = \tilde{b}_i(\vec{x}, t)$ and $d_i(\vec{x}, t) = b_i(\vec{x}, t) - \frac{\mu}{\sigma + \kappa} - C$. Here C is a counterterm which encodes the fluctuation corrections to the average concentrations. Owing to the cyclic symmetry among the three different species, we only need to introduce a single counterterm. The harmonic part of the action in terms of the new fields \tilde{d}_i and d_i reads

$$\mathcal{A}_0^{\text{ML}} = \sum_i \int dt d^d x \left[\tilde{d}_i \left(\partial_t - D\nabla^2 + \frac{\kappa\mu}{\kappa + \sigma} + (2\kappa + \sigma)C \right) d_i + \left(\frac{\sigma\mu}{\kappa + \sigma} + \sigma C \right) \tilde{d}_i d_{i+1} \right]. \quad (36)$$

Since the counterterm C is of first order in the perturbative expansion parameters, up to zeroth order the harmonic part of the action can be diagonalized by the following linear transformation

$$\begin{pmatrix} \tilde{d}_1 \\ \tilde{d}_2 \\ \tilde{d}_3 \end{pmatrix} = \frac{1}{\sqrt{3}} \begin{pmatrix} 1 & -\frac{1-i\sqrt{3}}{2} & -\frac{1+i\sqrt{3}}{2} \\ 1 & -\frac{1+i\sqrt{3}}{2} & -\frac{1-i\sqrt{3}}{2} \\ 1 & 1 & 1 \end{pmatrix} \begin{pmatrix} \tilde{\psi}_o \\ \tilde{\psi}_+ \\ \tilde{\psi}_- \end{pmatrix}, \quad (37)$$

and

$$\begin{pmatrix} d_1 \\ d_2 \\ d_3 \end{pmatrix} = \frac{1}{\sqrt{3}} \begin{pmatrix} 1 & -\frac{1+i\sqrt{3}}{2} & -\frac{1-i\sqrt{3}}{2} \\ 1 & -\frac{1-i\sqrt{3}}{2} & -\frac{1+i\sqrt{3}}{2} \\ 1 & 1 & 1 \end{pmatrix} \begin{pmatrix} \psi_o \\ \psi_+ \\ \psi_- \end{pmatrix}. \quad (38)$$

After applying this linear transformation, the action can be expressed as $\mathcal{A}^{\text{ML}} = \mathcal{A}_0^{\text{ML}} + \mathcal{A}_s^{\text{ML}} + \mathcal{A}_{\text{int}}^{\text{ML}}$, representing, respectively, the harmonic, source, and non-linear interaction terms. Again, we omit the four-point vertices, since they will not contribute to the dispersion relation renormalizations at one-loop order. The other terms are

$$\begin{aligned} \mathcal{A}_0^{\text{ML}} = \int dt d^d x & \left[\tilde{\psi}_o (\partial_t - D\nabla^2 + \mu + 2(\sigma + \kappa)C) \psi_o + \tilde{\psi}_+ (\partial_t - D\nabla^2 + \gamma_0 + i\nu_0) \psi_+ \right. \\ & + \tilde{\psi}_- (\partial_t - D\nabla^2 + \gamma_0 - i\nu_0) \psi_- \\ & \left. + \frac{1}{2} (\sigma + 4\kappa + i\sqrt{3}\sigma) C \tilde{\psi}_+ \psi_+ + \frac{1}{2} (\sigma + 4\kappa - i\sqrt{3}\sigma) C \tilde{\psi}_- \psi_- \right], \end{aligned} \quad (39)$$

$$\begin{aligned} \mathcal{A}_s^{\text{ML}} = \int dt d^d x & \left[(\mu C + (\kappa + \sigma)C^2) (\sqrt{3}\tilde{\psi}_o + \tilde{\psi}_o^2) \right. \\ & \left. + \left(-\frac{3\mu^2\sigma}{(\kappa + \sigma)^2} + 2\mu\frac{\kappa - 2\sigma}{\kappa + \sigma} C + (2\kappa - \sigma)C^2 \right) \tilde{\psi}_+ \tilde{\psi}_- \right], \end{aligned} \quad (40)$$



Figure 6. Contributions to $\langle \psi_o \rangle$ in the ML model up to one-loop order. The solid lines represent the ψ_{\pm} modes as indicated, while the dashed lines denotes the ψ_o mode.

$$\begin{aligned}
\mathcal{A}_{\text{int}}^{\text{ML}} = \int dt d^d x \left[\left(\frac{\mu(\kappa - 2\sigma)}{\sqrt{3}(\kappa + \sigma)} + \frac{2\kappa - \sigma}{\sqrt{3}} C \right) (\tilde{\psi}_+^2 \psi_- + \tilde{\psi}_-^2 \psi_+) + \frac{\kappa + \sigma}{\sqrt{3}} \tilde{\psi}_o \psi_o^2 \right. \\
+ \left(\frac{\mu}{\sqrt{3}} + \frac{2(\kappa + \sigma)}{\sqrt{3}} C \right) \tilde{\psi}_o^2 \psi_o + \left(\frac{\mu(2\kappa - \sigma)}{\sqrt{3}(\kappa + \sigma)} + \frac{4\kappa + \sigma}{\sqrt{3}} C \right) (\tilde{\psi}_o \tilde{\psi}_+ \psi_+ + \tilde{\psi}_o \tilde{\psi}_- \psi_-) \\
+ \frac{\sqrt{3}}{6} (2\kappa - \sigma + \sqrt{3}i\sigma) \tilde{\psi}_- \psi_+^2 + \frac{\sqrt{3}}{6} (2\kappa - \sigma - \sqrt{3}i\sigma) \tilde{\psi}_+ \psi_-^2 + \frac{2\kappa - \sigma}{\sqrt{3}} \tilde{\psi}_o \psi_+ \psi_- \\
\left. + \frac{\sqrt{3}}{6} (4\kappa + \sigma - \sqrt{3}i\sigma) \tilde{\psi}_- \psi_o \psi_- + \frac{\sqrt{3}}{6} (4\kappa + \sigma + \sqrt{3}i\sigma) \tilde{\psi}_+ \psi_o \psi_+ + \text{four-point vertices} \right], \tag{41}
\end{aligned}$$

where $\gamma_0 = \mu(2\kappa - \sigma)/2(\sigma + \kappa)$ and $\nu_0 = \sqrt{3}\mu\sigma/2(\sigma + \kappa)$. The ψ_o mode corresponds to the fluctuation of the total particle density and decays exponentially at tree level. In contrast to the RPS model, the ML ψ_{\pm} modes display non-vanishing dissipation γ_0 already on the mean-field level. As mentioned above, a Hopf bifurcation occurs at $2\kappa = \sigma$; when $2\kappa < \sigma$, the system is unstable and spiral structures are spontaneously generated. In the perturbative regime, the assumed tiny fluctuation corrections should not change the overall stability features, but will only shift the Hopf bifurcation point by a small amount.

3.4. One-loop fluctuation corrections

Prior to calculating the renormalized quantities, we need to determine the counterterm C by requiring the average fluctuation of the total density to be zero, $\langle \psi_o \rangle = 0$. Up to one-loop order, the contributions to $\langle \psi_o \rangle$ are shown in Fig. 6. We note that the second diagram in Fig. 6 is of second order and thus can be dropped. The corresponding analytic expression results in

$$C = -\frac{\mu\sigma(2\kappa - \sigma)}{2D(\kappa + \sigma)^2} \int_k \frac{1}{k^2 + \frac{\gamma_0}{D}}. \tag{42}$$

We may now proceed to the fluctuation renormalization of the two-point vertex functions $\Gamma_{\tilde{\psi}_o \psi_o}^{(1,1)}$ and $\Gamma_{\tilde{\psi}_{\pm} \psi_{\pm}}^{(1,1)}$, which encode the self-energies entering the dispersion relation of the ψ_o and ψ_{\pm} modes. As the total particle number is not conserved in the ML model, the dispersion relation acquires non-trivial corrections from the perturbation expansion. The one-loop diagrams that contribute to the vertex function $\Gamma_{\tilde{\psi}_o \psi_o}^{(1,1)}$ are pictured in Fig. 7. The last diagram is of higher order and thus can be omitted; this

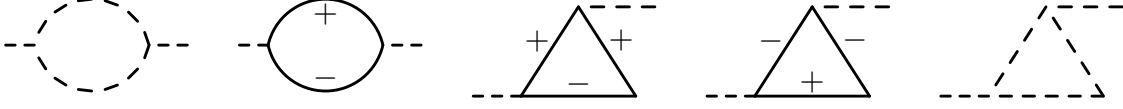


Figure 7. One-loop fluctuation contributions to the two-point vertex function $\Gamma_{\tilde{\psi}_o\psi_o}^{(1,1)}$ in the ML model.

results in

$$\begin{aligned} \Gamma_{\tilde{\psi}_o\psi_o}^{(1,1)}(p, \omega) &= i\omega + Dp^2 + \mu + 2(\kappa + \sigma)C - \frac{\mu(\kappa + \sigma)}{3D} \int_k I\left(\frac{\mu}{D}\right) \\ &\quad - \frac{2(\sigma + \kappa)\gamma_0}{3D\mu} (\gamma_0 - \sqrt{3}\nu_0) \int_k I\left(\frac{\gamma_0}{D}\right) - \frac{2\sqrt{3}(\sigma + \kappa)\gamma_0\nu_0}{3D^2\mu} (\gamma_0 + \mu) \int_k \frac{1}{k^2 + \frac{\gamma_0}{D}} I\left(\frac{\gamma_0}{D}\right). \end{aligned} \quad (43)$$

Provided $\gamma_0 > 0$, all corrections at one-loop level are real, and no imaginary part appears in the mass term of the ψ_o mode, hence there are no total particle number oscillations. However, for $\gamma_0 < 0$ the system exhibits emergent oscillations of the total particle number, indicating the spontaneous formation of spatio-temporal structures. As the renormalized two-point vertex function can also be written as

$$\Gamma_{\tilde{\psi}_o\psi_o}^{(1,1)}(p, \omega) = Z_{\phi_o} (i\omega + D_r^o p^2 + \mu_r), \quad (44)$$

the renormalized diffusivity D_r^o and mass parameter μ_r can be calculated accordingly. Here, Z_{ϕ_o} absorbs all wave function renormalizations. Since the rotating wave modes ψ_{\pm} acquires a different diffusivity renormalization from the o mode, we carefully distinguish the renormalized quantities D_r^{\pm} and D_r^o .

The explicit expressions for D_r^o and μ_r read

$$\begin{aligned} \mu_r &= \mu \left[1 - \frac{2(\sigma + \kappa)\gamma_0}{3D} \frac{1}{\mu} \int_k \frac{1}{k^2 + \frac{\gamma_0}{D}} - \frac{\sigma + \kappa}{3D} \int_k \frac{1}{k^2 + \frac{\mu}{D}} - \frac{\mu(\sigma + \kappa)}{6D^2} \int_k \frac{1}{(k^2 + \frac{\mu}{D})^2} \right. \\ &\quad \left. - \frac{(\sigma + \kappa)\gamma_0}{3D^2} \left(1 + \frac{2\sqrt{3}\nu_0\gamma_0}{\mu^2} \right) \int_k \frac{1}{(k^2 + \frac{\gamma_0}{D})^2} - \frac{\sqrt{3}(\sigma + \kappa)\nu_0\gamma_0(\gamma_0 + \mu)}{3D^3\mu} \int_k \frac{1}{(k^2 + \frac{\gamma_0}{D})^3} \right], \\ D_r^o &= D - \frac{\mu(\sigma + \kappa)}{3dD} \int_k \frac{k^2}{(k^2 + \frac{\mu}{D})^3} - \frac{2(\sigma + \kappa)\gamma_0}{3dD} \frac{1}{\mu} (\gamma_0 - \sqrt{3}\nu_0) \int_k \frac{k^2}{(k^2 + \frac{\gamma_0}{D})^3} \\ &\quad - \frac{2\sqrt{3}(\sigma + \kappa)\nu_0\gamma_0}{3dD^2} \frac{1}{\mu} (\gamma_0 + \mu) \int_k \frac{k^2}{(k^2 + \frac{\gamma_0}{D})^4}. \end{aligned} \quad (45)$$

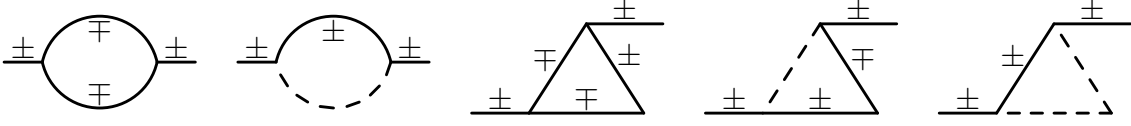


Figure 8. One-loop fluctuation contributions to the two-point vertex functions $\Gamma_{\tilde{\psi}_{\pm}\psi_{\pm}}^{(1,1)}$ in the ML model.

After evaluating the integrals one arrives at

$$\begin{aligned}
\mu_r &= 1 - \frac{\Gamma(1-d/2)}{2^d \pi^{d/2}} \left(\frac{\sigma + \kappa}{3D} \left(\frac{\mu}{D} \right)^{d/2-1} + \frac{2(\sigma + \kappa)\gamma_0}{3D\mu} \left(\frac{\gamma_0}{D} \right)^{d/2-1} \right) \\
&\quad - \frac{\Gamma(2-d/2)}{2^d \pi^{d/2}} \left[\frac{\mu(\sigma + \kappa)}{6D^2} \left(\frac{\mu}{D} \right)^{d/2-2} + \frac{(\sigma + \kappa)\gamma_0}{3D^2} \left(1 + \frac{2\sqrt{3}\nu_0\gamma_0}{\mu^2} \right) \left(\frac{\gamma_0}{D} \right)^{d/2-2} \right] \\
&\quad - \frac{\Gamma(3-d/2)}{2^d \pi^{d/2}} \frac{\sqrt{3}(\sigma + \kappa)\nu_0\gamma_0}{3D^3\mu} (\gamma_0 + \mu) \left(\frac{\gamma_0}{D} \right)^{d/2-3}, \\
D_r^o &= D - \frac{\Gamma(2-d/2)}{2^{d+2}\pi^{d/2}} \left[\frac{\mu(\sigma + \kappa)}{3D} \left(\frac{\mu}{D} \right)^{d/2-2} + \frac{2(\sigma + \kappa)\gamma_0}{3D\mu} (\gamma_0 - \sqrt{3}\nu_0) \left(\frac{\gamma_0}{D} \right)^{d/2-2} \right] \\
&\quad - \frac{\Gamma(3-d/2)}{3 \cdot 2^{d+2}\pi^{d/2}} \frac{2\sqrt{3}(\sigma + \kappa)}{3D^2\mu} \nu_0\gamma_0(\gamma_0 + \mu) \left(\frac{\gamma_0}{D} \right)^{d/2-3}.
\end{aligned} \tag{46}$$

For $d \geq 2$, UV divergences in μ_r are manifest; but since the lattice constant c serves as a natural UV cutoff in lattice models, we will not discuss these UV divergences further.

The renormalized vertex function $\Gamma_{\tilde{\psi}_{\pm}\psi_{\pm}}^{(1,1)}$ can also be calculated according to the one-loop diagrams in Fig. 8, resulting in

$$\begin{aligned}
\Gamma_{\tilde{\psi}_{\pm}\psi_{\pm}}^{(1,1)}(p, \omega) &= i\omega + Dp^2 + \gamma_0 \pm i\nu_0 + \frac{\sigma + \kappa}{\mu} (\gamma_0 + \mu \pm i\nu_0) C \\
&\quad - \frac{(\kappa + \sigma)(\gamma_0 - \sqrt{3}\nu_0)}{3D\mu} (\gamma_0 \mp i\nu_0) \int_k I\left(\frac{\gamma_0 \mp i\nu_0}{D}\right) \\
&\quad - \frac{(\sigma + \kappa)\gamma_0}{3D\mu} (\gamma_0 + \mu \pm i\nu_0) \int_k I\left(\frac{\gamma_0 + \mu \pm i\nu_0}{2D}\right) \\
&\quad - \frac{2\sqrt{3}(\sigma + \kappa)\nu_0}{3D^2\mu} (\gamma_0^2 + \nu_0^2) \int_k \frac{1}{k^2 + \frac{\gamma_0}{D}} I\left(\frac{\gamma_0 \mp i\nu_0}{D}\right) \\
&\quad - \frac{\sqrt{3}(\sigma + \kappa)\gamma_0\nu_0}{3D^2\mu} (\gamma_0 + \mu \pm i\nu_0) \int_k \frac{1}{k^2 + \frac{\gamma_0}{D}} I\left(\frac{\gamma_0 + \mu \pm i\nu_0}{2D}\right).
\end{aligned} \tag{47}$$

Upon invoking the relation with renormalized quantities

$$\Gamma_{\tilde{\psi}_{\pm}\psi_{\pm}}^{(1,1)}(p, \omega) = Z_{\phi_{\pm}} (i\omega + D_r^{\pm} p^2 + \gamma_r \pm i\nu_r), \tag{48}$$

the expressions for the renormalized parameters γ_r and ν_r are readily inferred,

$$\begin{aligned}
\gamma_r \pm i\nu_r = \gamma_0 \pm i\nu_0 + (\sigma + \kappa) & \left[M_1^{(\pm)} \frac{\Gamma(1-d/2)}{2^d \pi^{d/2}} \left(\frac{\gamma_0}{D} \right)^{d/2-1} \right. \\
& + M_2^{(\pm)} \frac{\Gamma(1-d/2)}{2^d \pi^{d/2}} \left(\frac{\gamma_0^2 + \nu_0^2}{D^2} \right)^{(d-2)/4} \exp\left(\mp i \frac{d-2}{2} \theta \right) \\
& + M_3^{(\pm)} \frac{\Gamma(1-d/2)}{2^d \pi^{d/2}} \left(\frac{(\mu + \gamma_0)^2 + \nu_0^2}{4D^2} \right)^{(d-2)/4} \exp\left(\pm i \frac{d-2}{2} \eta \right) \\
& + M_4^{(\pm)} \frac{\Gamma(2-d/2)}{2^d \pi^{d/2}} \left(\frac{\gamma_0^2 + \nu_0^2}{D^2} \right)^{(d-4)/4} \exp\left(\mp i \frac{d-4}{2} \theta \right) \\
& \left. + M_5^{(\pm)} \frac{\Gamma(2-d/2)}{2^d \pi^{d/2}} \left(\frac{(\mu + \gamma_0)^2 + \nu_0^2}{4D^2} \right)^{(d-4)/4} \exp\left(\pm i \frac{d-4}{2} \eta \right) \right], \tag{49}
\end{aligned}$$

where the coefficients $M_i^{(\pm)}$ are defined in Eq. (B.2) in the appendix, and the angles θ and η are given by $\tan \theta = \nu_0/\gamma_0$ and $\tan \eta = \nu_0/(\gamma_0 + \mu)$. We note that at odd dimensions d , the first term in the bracket in Eq. (49) switches from real to imaginary as γ_0 changes its sign; however, at even dimensions, this term is always real. Finally, the renormalized diffusivity reads

$$\begin{aligned}
D_r^\pm = D - \frac{\kappa + \sigma}{d 2^d \pi^{d/2}} & \left[\Gamma(1-d/2) P_1^{(\pm)} \left(\frac{\gamma_0^2 + \nu_0^2}{D^2} \right)^{(d-2)/4} \exp\left(\mp i \frac{d-2}{2} \theta \right) \right. \\
& + \Gamma(2-d/2) P_2^{(\pm)} \left(\frac{\gamma_0^2 + \nu_0^2}{D^2} \right)^{(d-4)/4} \exp\left(\mp i \frac{d-4}{2} \theta \right) \\
& + \frac{\Gamma(3-d/2)}{2} P_3^{(\pm)} \left(\frac{\gamma_0^2 + \nu_0^2}{D^2} \right)^{(d-6)/4} \exp\left(\mp i \frac{d-6}{2} \theta \right) \\
& + \Gamma(1-d/2) Q_1^{(\pm)} \left(\frac{(\mu + \gamma_0)^2 + \nu_0^2}{4D^2} \right)^{(d-2)/4} \exp\left(\pm i \frac{d-2}{2} \eta \right) \\
& + \Gamma(2-d/2) Q_2^{(\pm)} \left(\frac{(\mu + \gamma_0)^2 + \nu_0^2}{4D^2} \right)^{(d-4)/4} \exp\left(\pm i \frac{d-4}{2} \eta \right) \\
& + \frac{\Gamma(3-d/2)}{2} Q_3^{(\pm)} \left(\frac{(\mu + \gamma_0)^2 + \nu_0^2}{4D^2} \right)^{(d-6)/4} \exp\left(\pm i \frac{d-6}{2} \eta \right) \\
& \left. - \Gamma(1-d/2) \left(P_1^{(\pm)} + Q_1^{(\pm)} \right) \left(\frac{\gamma_0}{D} \right)^{(d-2)/2} \right]. \tag{50}
\end{aligned}$$

In the appendices, we provide additional details and the definitions of the various coefficients, as well as explicit evaluations for $d = 1, 2, 3$. Here, we focus on the behavior of the damping parameter μ_r across different dimensions. It is important to note that μ_r is generally a complex number: Its imaginary part conveys information about spatial oscillations, while its real part represents either exponential decay or growth of the average particle density.

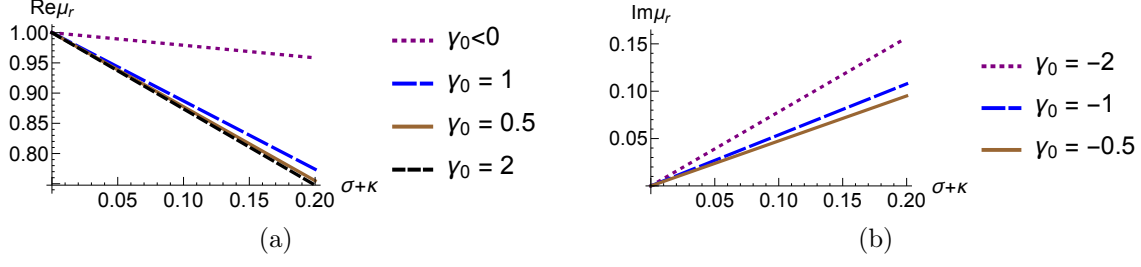


Figure 9. Renormalized μ_r in one dimension ($d = 1$): (a) Real part of μ_r as a function of $\sigma + \kappa$ with $D = 1$, $\mu = 1$, $\nu_0 = 1$, and different values of γ_0 . (b) Imaginary part of u_r as a function of λ with $D = 1$, $\mu = 1$, $\nu_0 = 1$, and different $\gamma_0 < 0$.

3.4.1. $d = 1$: In one dimension, the renormalized damping parameter μ_r reads

$$\mu_r = \mu \left[1 - \frac{5(\sigma + \kappa)}{24D} \sqrt{\frac{D}{\mu}} - \frac{\sigma + \kappa}{D} \sqrt{\frac{D}{\gamma_0}} \left(\frac{1}{12} + \frac{\gamma_0}{3\mu} + \frac{\sqrt{3}\nu_0}{16\mu} + \frac{\sqrt{3}\nu_0}{16\gamma_0} + \frac{\sqrt{3}\nu_0\gamma_0}{6\mu^2} \right) \right]. \quad (51)$$

For $\gamma_0 < 0$, μ_r acquires an imaginary part, indicating oscillatory behavior. However, if $\gamma_0 > 0$, there is only damping. We display different scenarios in Fig. 9.

3.4.2. $d = 2$: At two dimensions, we need to introduce the UV cutoff $\Lambda \sim \pi/c$; the damping parameter becomes

$$\mu_r = \mu \left[1 - \frac{\sigma + \kappa}{6D\pi} \frac{\gamma_0}{\mu} \ln \frac{D\Lambda^2}{\gamma_0} - \frac{\sigma + \kappa}{12D\pi} \ln \frac{D\Lambda^2}{\mu} - \frac{\sigma + \kappa}{24D\pi} - \frac{\sigma + \kappa}{12D\pi} \left(1 + \frac{\sqrt{3}\nu_0}{2\mu} + \frac{\sqrt{3}\nu_0}{2\gamma_0} + \frac{2\sqrt{3}\nu_0\gamma_0}{\mu^2} \right) \right]. \quad (52)$$

As in the one-dimensional case, when $\gamma_0 > 0$, we have pure damping, whereas the system displays population oscillations if $\gamma_0 < 0$. The damping coefficients μ_r at $d = 2$ for different bare parameters are plotted in Fig. 10.

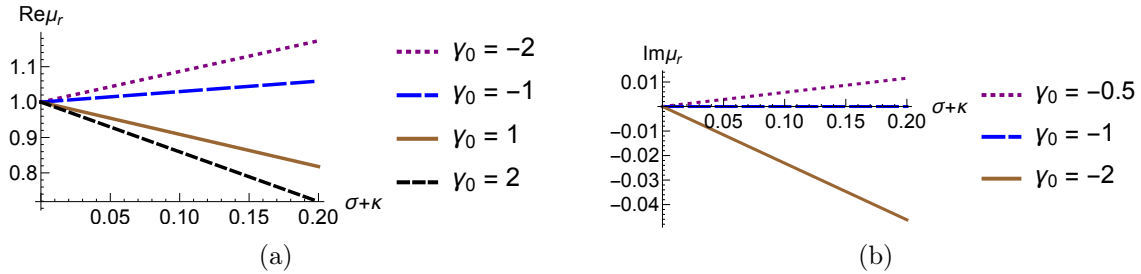


Figure 10. Renormalized μ_r at two dimensions ($d = 2$) with cutoff $\Lambda^2 = 10000$: (a) Real part of μ_r as a function of $\sigma + \kappa$ with $D = 1$, $\mu = 1$, $\nu_0 = 1$, and different values of γ_0 . (b) Imaginary part of u_r as a function of λ with $D = 1$, $\mu = 1$, $\nu_0 = 1$, and different $\gamma_0 < 0$.

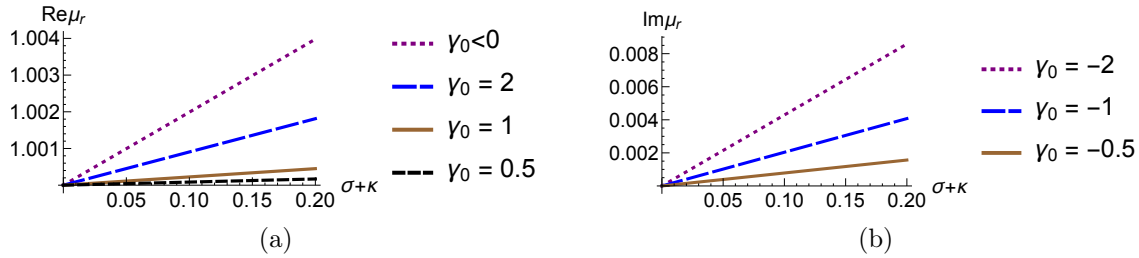


Figure 11. Renormalized μ_r at three dimensions ($d = 3$): (a) Real part of μ_r as a function of $\sigma + \kappa$ with $D = 1$, $\mu = 1$, $\nu_0 = 1$, and different values of γ_0 . (b) Imaginary part of u_r as a function of λ with $D = 1$, $\mu = 1$, $\nu_0 = 1$, and different $\gamma_0 < 0$.

3.4.3. $d = 3$: In three dimensions, the damping parameter reads

$$\mu_r = \mu \left[1 + \frac{\sigma + \kappa}{16D\pi} \sqrt{\frac{\mu}{D}} + \frac{\sigma + \kappa}{6D\pi} \sqrt{\frac{\gamma_0}{D}} \left(-\frac{1}{4} + \frac{\gamma_0}{\mu} - \frac{\sqrt{3}\nu_0}{16\mu} - \frac{\sqrt{3}\nu_0}{16\gamma_0} - \frac{\sqrt{3}\nu_0\gamma_0}{2\mu^2} \right) \right]. \quad (53)$$

Again, oscillations emerge in the region where $\gamma_0 < 0$. The real and imaginary parts of the damping parameter μ are depicted in Fig. 11.

For $\nu_0 = 1$, the damping μ_r decreases in one and two dimensions, but increases in three dimensions in the stable region where $\gamma_0 > 0$, as shown in Figs. 9, 10, and 11. This indicates that the reactions effectively slow down the relaxation processes in one and two dimensions, but speed them up in three dimensions. However, due to the highly nonlinear dependence on the parameters μ_0 , γ_0 , and ν_0 , a more general conclusion cannot be made. It is worth noting that in the unstable region, an imaginary part of μ_r is generated, formally resulting from the subtraction of an inadequate homogeneous steady state. Yet these emergent oscillations manifestly indicate the instability with respect to spontaneous formation of spatio-temporal patterns in this regime. We emphasize again that the one-loop fluctuation corrections should merely induce small quantitative corrections, and cannot induce qualitative changes in the region where perturbation theory is applicable. The ML system thus maintains a bifurcation point, below which the homogeneous ground state is rendered unstable and spiral structures emerge.

4. Comparison between the RPS, ML, and LV models

In this section, we present a thorough comparison between the spatically extended stochastic LV, RPS, and ML models. We specifically discuss the spontaneous formation of spatio-temporal structures and the stability of the homogeneous state up to perturbative one-loop order in the fluctuation corrections. We also briefly address the influence of quenched spatial disorder in the reaction rates in the perturbative regime.

4.1. Spiral formation from a single lattice site point of view

It is well-established that in sufficiently large spatial systems, the ML model displays spontaneously emerging dynamic spiral structures in individual simulation runs (these

are of course averaged out in ensemble averages). Here, we propose that one crucial necessary condition for the formation of such persistent spatio-temporal patterns is the existence of a stable and uniform oscillation frequency at the local lattice site level, which then allows spatially extended coherent oscillatory features.

Each site in a lattice subject to stochastic reactions and spreading processes can be regarded as a separate system that is coupled to a particle reservoir (in the thermodynamic limit). In the ML model, at the (linearized) mean-field level, the local oscillation frequency is uniquely determined by the reaction rates, as is also apparent in the diagonalized ML Doi–Peliti action (39) at tree level. A similar definition of the oscillation frequency at linearized mean field level can also be obtained in the LV model [34]. However, in the RPS model at tree level, the oscillation frequency is set by the global conserved particle number ρ . As the particle number at each site is changing all the time owing to its coupling to the environment that serves as a nonlocal reservoir, there does not exist a unique characteristic oscillation frequency for each site during any single run stochastic realization. The average of the oscillation frequency with a fixed total particle number is given by the the expression in the diagonalized RPS Doi–Peliti action (18).

These straightforward tree-level arguments are readily generalized to all (loop) orders in the perturbation expansion. In the ML model, no nonlinear terms that depend on the total particle density (or any other global quantity) are present in the action, and thus the renormalized frequency will also be independent of the particle number density. This is not the case for the RPS model, where ρ manifestly enters the vertices. A perhaps more straightforward way to understand this distinction invokes the fixed points (stationary species densities) of the systems. In the RPS system, there exists a fixed line that is parameterized by the conserved total particle number. For each lattice site in the RPS model, the population oscillations wander along this fixed line with a mean that corresponds to the averaged local total particle number at this specific site. In contrast, the ML and LV models have unique fixed points, independent of any global constraints that originate from conservation laws, and consequently all lattice sites are governed by identical oscillation frequencies determined by these fixed points.

To illustrate these points, we plot the time evolution of the population density of a single species at two randomly chosen lattice sites in a single simulation run for the RPS and ML models in Figs. 12 and 13, respectively. For the RPS species density, the time intervals separating different peaks are not regularly spaced for the two lattice sites. Correspondingly, its Fourier transform displays multiple peaks with almost equal intensities, and no well-defined characteristic frequency is discernible. In contrast, the peaks in the ML species density time evolution are evenly separated, and hence a dominant Fourier peak emerges. These numerical observations support our analysis that the frequency in a single run in the ML model is well-defined, while that is clearly not the case for the RPS system. Yet a well-defined oscillation frequency clearly constitutes a necessary condition to form spatio-temporal patterns.

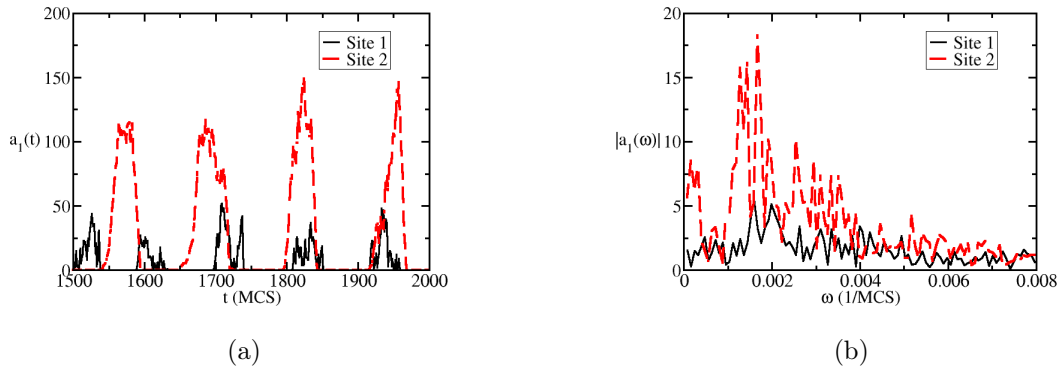


Figure 12. (a) Time evolution of the density of species A_1 in the RPS model on two randomly chosen sites; (b) frequency spectrum of the time series in (a) obtained through a Fourier transform. The simulation was run with a reaction rate 0.5 and on a lattice with 100×100 sites. The reactions in the simulation take place off-site and no additional hopping processes are incorporated.

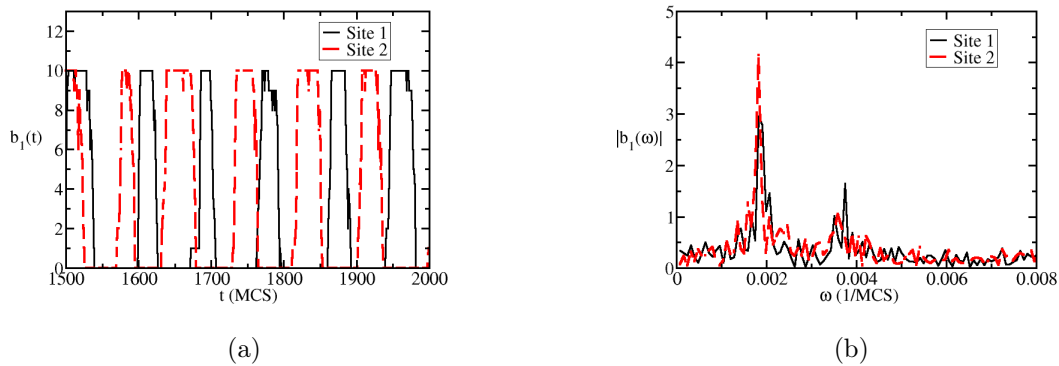


Figure 13. (a) Time evolution of the density of species B_1 in the ML model on two randomly chosen sites; (b) frequency spectrum of the time series in (a) obtained through a Fourier transform. In the simulation, the predation and reproduction rates are both set to 0.5 and the system size is 100×100 lattice sites. The reactions in the simulation take place off-site, and no additional hopping processes are incorporated.

4.2. Stability of the homogeneous ground states against fluctuations (to one-loop order)

While we posit above that a stable oscillation frequency at each lattice site is a necessary requirement to form oscillatory spatio-temporal patterns such as spirals, this is not a sufficient condition. Another crucial ingredient is of course that the spatially homogeneous stationary state is rendered unstable; fluctuations of a certain wavevector range will then spontaneously generate spatial patterns. [40, 41]

In the stochastic spatially extended LV model [34], in the absence of site restrictions, the population oscillation damping vanishes in the Gaussian approximation. To one-loop order, a negative damping frequency is generated which indicates an instability

of the spatially uniform system, inducing nontrivial particle transport that in turn drives the formation of expanding evasion-pursuit activity waves. In the ML model, the damping coefficient is already nonzero in the Gaussian approximation. As stated above, when $2\kappa < \sigma$, the limit cycles of the ML model become unstable and spiral structures emerge. Yet within the realm of a perturbative approach, any fluctuation corrections will only shift the Hopf bifurcation point, but cannot qualitatively change the system's overall features. In contrast, the RPS system behaves similarly to the LV system, as we encounter a vanishing damping coefficient in the Gaussian approximation. However, at one-loop level, the generated mass term is positive indicating merely a generated finite damping constant, as opposed to its negative counterpart in the LV model. Hence the RPS model remains inert against spontaneous pattern formation. Higher-order terms in the fluctuation expansion should not overturn the sign of the one-loop results within the perturbative regime, which renders this argument perturbatively robust.

4.3. Influence of quenched spatially disordered reaction rates

In this part, we briefly investigate the effect of spatially disordered, uniformly distributed quenched reaction probabilities on the fluctuation corrections. We start with the Doi–Peliti action

$$\mathcal{A} = \int dt d^d x [\mathcal{L}_0(\hat{a}_i, a_i) + \mathcal{L}'(\hat{a}_i, a_i)], \quad (54)$$

where \mathcal{L}_0 and \mathcal{L}' are (usually polynomial) functions of the fields $\{\hat{a}_i\}$ and $\{a_i\}$. We introduce spatial disorder to \mathcal{L}' , which we take to represent stochastic reactions while \mathcal{L}_0 encodes particle diffusions. The action with quenched spatial disorder is then given by

$$\mathcal{A}_D = \int dt d^d x \mathcal{L}_0 + \int d^d x \eta(\vec{x}) \int d\mathcal{L}'; \quad (55)$$

here, we assume $\eta(\vec{x})$ to be uniformly distributed in the interval $[0, 2]$ with mean $\bar{\eta} = 1$. Note that the reaction rates are only spatially disordered and remain fixed in time. The average of any observables follows from Eq. (A.9) through

$$\overline{\langle O(t) \rangle} \propto \prod_{\vec{x}} \int_0^2 \frac{d\eta(\vec{x})}{2} \int \prod_i \mathcal{D}[\hat{a}_i] \mathcal{D}[a_i] O(\{\hat{a}_i, a_i\}) e^{-\mathcal{A}_D}, \quad (56)$$

where the overline denotes the quenched disorder average. We can readily integrate out the disorder $\eta(\vec{x})$ first, since the observable O is independent of the random variables η , and arrive at

$$\overline{\langle O(t) \rangle} \propto \int \prod_i \mathcal{D}[\hat{a}_i] \mathcal{D}[a_i] O(\{\hat{a}_i, a_i\}) e^{-\mathcal{A}'_D}, \quad (57)$$

with

$$\mathcal{A}'_D = \mathcal{A} + \int d^d x \ln \left[\frac{\sinh(\int dt \mathcal{L}')}{\int dt \mathcal{L}'} \right]. \quad (58)$$

Incorporating disorder in the original Doi–Peliti action (54) thus effectively leads to an additional term that is nonlocal in the time domain, owing to the temporally fixed

reaction rates. However, in the perturbative regime where \mathcal{L}' is small, this extra term can be expanded near $\mathcal{L}' = 0$:

$$\ln \left[\frac{\sinh(\int dt \mathcal{L}')}{\int dt \mathcal{L}'} \right] = \frac{1}{3} \int dt dt' \mathcal{L}'_t \mathcal{L}'_{t'} + \mathcal{O}(\mathcal{L}'^3), \quad (59)$$

where the labels t and t' distinguish the different time dependences. It is evident from this expansion that the extra temporally nonlocal term “entangles” different replicas of the system. However, as the first term is already second-order in \mathcal{L}' , it is of higher order than the original action \mathcal{A} , and should not markedly affect the system’s fluctuation corrections in the naive perturbation regime, at least to low loop orders. This observation may account for the insensitivity of the RPS and ML models to quenched randomness in the reaction rates, as reported in Refs. [10, 13]. We remark that the stronger effects of varying predation rates λ in the LV system can be largely traced to the sensitivity $\sim 1/\lambda$ of the stationary species densities already on the mean-field approximation level [31].

5. Summary and conclusions

In this paper, we have investigated the dynamics of the RPS and ML models up to one-loop order in the fluctuation corrections by means of a perturbative field-theoretical analysis. We utilized the Doi–Peliti formalism to obtain the dynamical probability functional for the stochastic Markovian dynamics, and also extracted the equivalent generalized Langevin equations. In the Gaussian theory, as expected, the RPS model displays only purely oscillatory modes in addition to the strictly diffusive conserved total particle density. In the ML model, a Hopf bifurcation point appears at $2\kappa - \sigma = 0$ that separates the parameter space into stable and unstable regions; in the latter regime, spiral structures are spontaneously generated.

The one-loop fluctuation corrections in the RPS model generate dissipation. We have found that in the physically accessible dimensions $d = 1, 2, 3$, the damping coefficient is always positive. This indicates the stability of the spatially uniform stationary state in the RPS model, at least in the perturbative regime. Thus, our analysis sheds light on the absence of spatio-temporal structures in the RPS model. In addition, the one-loop correction to the oscillation frequency is IR divergent due to the dissipation-free nature of the mean-field modes, very similar to the LV model. However, outside the range of validity of the perturbation expansion, the damping terms become sizeable; hence we argue that this IR divergence becomes naturally regularized. This explains why no significant fluctuation corrections to the oscillation frequency have as yet been numerically observed in computer simulations, which have invariably been situated far away from the perturbative regime.

In the ML model, as both the dissipation and oscillation frequencies are already finite at mean-field level, the one-loop fluctuation corrections should not qualitatively modify the mean-field conclusions. Since both propagating modes are massive due to

the finite damping coefficients, the ML system does not display any IR singularities. Hence the ML model is insensitive to fluctuations at least perturbatively, and in the region where the homogeneous steady state is stable. Moreover, we have argued that uniformly distributed quenched random disorder in the reaction rates only weakly influences fluctuation corrections in either system, which is in agreement with earlier Monte Carlo simulation data.

Finally, we provided two decisive criteria that determine the possibility of spatio-temporal structures in the LV, RPS, and ML models. The first argument considers a single lattice site point of view, while the second is based on studying the global stability of the spatially homogeneous stationary state of the system. From a single lattice site perspective, a necessary (but not sufficient) condition for the emergence of spatially extended coherent oscillatory behavior is that the oscillation frequency is constant over space and time in each run. Different oscillation frequencies on distinct sites would not allow the formation of stable coherent patterns. From a global point of view, only if the spatially uniform quasi-steady state is unstable against finite-wavelength fluctuations can non-trivial spatio-temporal structures be generated, as is evident in the ML model. Both these criteria explain the absence of spatio-temporal patterns in the RPS system, as a consequence of the relevant conservation law for the total particle number, in contrast with the otherwise apparently similar LV and ML models.

Acknowledgments

The authors gratefully acknowledge inspiring discussions with Erwin Frey, Nigel Goldenfeld, Qian He, Mauro Mobilia, Michel Pleimling, Alastair Rucklidge, and Royce K. P. Zia. This research was partially supported by the U.S National Science Foundation, Division of Mathematical Sciences under Award No. NSF DMS-2128587.

Appendix A. Doi–Peliti formalism and the asymmetric RPS model

In this appendix, we provide a brief overview of the construction of the time evolution operator and the resulting field-theoretic action via the Doi–Peliti mapping of stochastic reactions to a non-Hermitean many-body quantum action [42, 43, 44, 45] (for recent reviews and additional details, see Refs. [35, 36, 46, 47]). We then proceed to construct coupled Langevin equations describing the dynamics of the system similar to previous work in the context of the LV system [28, 34, 35], plankton-based predator-prey models [48], and Turing patterns [49]. An interesting corner limit is analyzed via the generalized Langevin equations; we will show that the strongly asymmetric RPS system reduces to an effective LV model. Finally, we construct the diagonalized action for the RPS model and briefly compare the general situation with the symmetric version discussed in the bulk of this paper. This appendix is written in a self-consistent way and we hope it will be of use to readers who would like to delve into the Doi–Peliti formalism.

Appendix A.1. Stochastic time evolution operator

The RPS rules (1) mandate that particle numbers are discrete, hence the occupation numbers of lattice sites can be written as positive integers $n_{i\alpha}$, where the index i accounts for different particle species, while α enumerates the sites on a d -dimensional hyper-cubic lattice. The master equation for the local, on-site RPS reactions then reads:

$$\frac{\partial P(n_{i\alpha}; t)}{\partial t} = \sum_{i=1,2,3} \lambda'_i [(n_{i\alpha} - 1)(n_{i+1\alpha} + 1)P(n_{i\alpha} - 1, n_{i+1\alpha} + 1; t) - n_{i\alpha}n_{i+1\alpha}P(n_{i\alpha}, n_{i+1\alpha}; t)] , \quad (\text{A.1})$$

where the index i wraps around (i.e., $i = 4$ is to be identified with $i = 1$). Note that for brevity we have not included hopping to adjacent lattice sites here. As an initial state, we assume a uniform distribution of particles with an average initial number of particles N_i per lattice site of species i . This corresponds to a Poisson distribution for the occupation number of each species i at all lattice sites α , $P(n_{i\alpha}; t) = \prod_{i=1,2,3} N_i^{n_{i\alpha}} e^{-N_i} / (n_{i\alpha}!)$. The discrete nature of the possible states of the RPS systems suggests the introduction of a product Fock space state vector

$$|\Phi(t)\rangle = \sum_{\{n_{i\alpha}\}} P(n_{i\alpha}; t) \prod_{i=1,2,3} \prod_{\alpha=1}^{L^d} |n_{i\alpha}\rangle , \quad (\text{A.2})$$

where the $|n_{i\alpha}\rangle$ represent the occupation states of species i on lattice site α . In analogy with the quantum-mechanical harmonic oscillator, the single-site states (and thereby the full state vector) can be acted upon by bosonic ladder operators obeying the commutation relations $[a_{i\alpha}, a_{j\beta}] = 0$ and $[a_{i\alpha}, a_{j\beta}^\dagger] = \delta_{\alpha\beta} \delta_{ij}$. The occupation number eigenstates are constructed via $a_{i\alpha}|n_{i\alpha}\rangle = n_{i\alpha}|n_{i\alpha} - 1\rangle$, $a_{i\alpha}^\dagger|n_{i\alpha}\rangle = |n_{i\alpha} + 1\rangle$, and the empty state $|0\rangle$ is defined by $a_{i\alpha}|0\rangle = 0$.

The time evolution of the state vector (A.2) follows directly from the master equation (A.1) and can be written in the form

$$\frac{\partial}{\partial t} |\Phi(t)\rangle = -H |\Phi(t)\rangle \iff |\Phi(t)\rangle = e^{-Ht} |\Phi(0)\rangle , \quad (\text{A.3})$$

where H denotes the (time-independent) Liouville operator which can be split into a diffusion and a reaction term, $H = H_{\text{diff}} + H_{\text{reac}}$, where the on-site reaction contribution is a sum of local terms $H_{\text{reac}} = \sum_{i=1}^{L^d} H_\alpha$, and specifically for the RPS model

$$H_\alpha = \sum_{i=1,2,3} \lambda'_i (a_{i+1\alpha}^\dagger - a_{i\alpha}^\dagger) a_{i\alpha}^\dagger a_{i\alpha} a_{i+1\alpha} . \quad (\text{A.4})$$

Similarly, since on-lattice diffusion is implemented by particles performing simple jumps between nearest-neighbor lattice sites, the diffusion part of H reads

$$H_{\text{diff}} = \sum_{i=1,2,3} \frac{D_i}{c^2} \sum_{\langle \alpha\beta \rangle} (a_{i\alpha}^\dagger - a_{i\beta}^\dagger) (a_{i\alpha} - a_{i\beta}) , \quad (\text{A.5})$$

where $\langle \alpha\beta \rangle$ indicates a sum over all possible nearest-neighbor lattice site pairs in the system.

Appendix A.2. Coherent-state path integral and equivalent Langevin partial differential equations

Following the steps of Refs. [34, 35, 36], we write averages for observables $O = O(\{n_{i\alpha}\})$ as a multi-dimensional integral over coherent states

$$\langle O(t) \rangle \propto \int \prod_{i=1,2,3} \prod_{\alpha=1}^{L^d} d\psi_{i\alpha}^* d\psi_{i\alpha} O(\{\psi_{i\alpha}\}) e^{-\mathcal{A}(\psi_{i\alpha}^*, \psi_{i\alpha}; t)}, \quad (\text{A.6})$$

where the $\psi_{i\alpha}$ and $\psi_{i\alpha}^*$ are complex eigenvalues describing the coherent right and left eigenstates of the ladder operators $a_{i\alpha}$ and $a_{i\alpha}^\dagger$, respectively. The coherent-state ‘‘action’’ is given by

$$\begin{aligned} \mathcal{A}(\psi_{i\alpha}^*, \psi_{i\alpha}; t') = & \sum_{i=1,2,3} \sum_{\alpha=1}^{L^d} \left[\int_0^{t'} dt \psi_{i\alpha}^*(t) \frac{\partial \psi_{i\alpha}(t)}{\partial t} dt - \psi_{i\alpha}(t') - N_i \psi_{i\alpha}^*(0) \right] \\ & + \int_0^{t'} dt H(a_{i\alpha}^\dagger \rightarrow \psi_{i\alpha}^*(t), a_{i\alpha} \rightarrow \psi_{i\alpha}(t)), \end{aligned} \quad (\text{A.7})$$

where we have to replace the ladder operators by their eigenvalues in the Liouville operator H .

In the spatial continuum limit (lattice constant $c \rightarrow 0$) we may replace the sum over lattice sites with a d -dimensional volume integral $\sum_{\alpha=1}^{L^d} \rightarrow c^{-d} \int d^d x$, and the discretely spaced coherent-state values with continuous fields $\psi_{i\alpha}(t) \rightarrow c^d a_i(\vec{x}, t)$ and $\psi_{i\alpha}^*(t) \rightarrow 1 + \tilde{a}_i(\vec{x}, t)$. Hence, the ‘‘bulk’’ part of action (not considering the terms from the initial conditions at $t = 0$ and the projection states at $t = t'$) of the RPS system is given by

$$\begin{aligned} \mathcal{A} = \int dt d^d x \left[\sum_{i=1,2,3} \tilde{a}_i \left(\partial_t - D_\alpha \nabla^2 \right) a_i + \lambda_1 a_1 a_2 (\tilde{a}_1 + 1) (\tilde{a}_2 - \tilde{a}_1) \right. \\ \left. + \lambda_2 a_2 a_3 (\tilde{a}_2 + 1) (\tilde{a}_3 - \tilde{a}_2) + \lambda_3 a_3 a_1 (\tilde{a}_3 + 1) (\tilde{a}_1 - \tilde{a}_3) \right]. \end{aligned} \quad (\text{A.8})$$

In the continuum limit we can thus write averages in the following coherent-state path integral form

$$\langle O(t) \rangle \propto \int \prod_{i=1,2,3} \mathcal{D}[\tilde{a}_i] \mathcal{D}[a_i] O(\{a_i\}) e^{-\mathcal{A}(\tilde{a}_i, a_i; t)}. \quad (\text{A.9})$$

Our aim here is to derive stochastic partial differential (Langevin) equations for the species concentrations that accurately capture the intrinsic reaction noise. To this end, we note that the Janssen–de Dominicis response functional [35, 37, 38, 50]

$$\mathcal{A} = \int dt d^d x \sum_i \tilde{a}_i \left(\partial_t a_i - D_i \nabla^2 a_i - F_i[\{a_i\}] - \sum_j L_{ij}[\{a_i\}] \tilde{a}_j \right) \quad (\text{A.10})$$

is equivalent to the set of SPDEs

$$\partial_t a_i = D_i \nabla^2 a_i(\vec{x}, t) + F_i[\{a_i(\vec{x}, t)\}] + \zeta_i(\vec{x}, t) , \quad (\text{A.11})$$

with the associated noise (cross-)correlations

$$\langle \zeta_i(\vec{x}, t) \zeta_j(\vec{x}', t') \rangle = 2L_{ij}[\{a_i(\vec{x}, t)\}] \delta(t - t') \delta(\vec{x} - \vec{x}') . \quad (\text{A.12})$$

This correspondence allows the immediate derivation of a coupled Langevin equation formulation of any system that exhibits an action functional of the form (A.10). Hence, via a direct comparison with the action of the RPS system (A.7), we can extract the deterministic part of the SPDEs describing the RPS system

$$F_1 = (\lambda_1 a_2 - \lambda_3 a_3) a_1 , \quad F_2 = (\lambda_2 a_3 - \lambda_1 a_1) a_2 , \quad F_3 = (\lambda_3 a_1 - \lambda_2 a_2) a_3 , \quad (\text{A.13})$$

which equal the right-hand side of the mean-field equations, as they should. Furthermore, the effective noise correlations are given by the matrix L_{ij} :

$$\begin{aligned} L_{11} &= \lambda_1 a_1 a_2 , & L_{12} &= -\frac{\lambda_1}{2} a_1 a_2 , & L_{13} &= -\frac{\lambda_3}{2} a_1 a_3 , \\ L_{22} &= \lambda_2 a_2 a_3 , & L_{23} &= -\frac{\lambda_2}{2} a_2 a_3 , & L_{33} &= \lambda_3 a_1 a_3 . \end{aligned} \quad (\text{A.14})$$

Hence, the SPDEs (A.11) can be constructed from the mean-field equations by including a term that accounts for diffusion and multiplicative noise terms obeying the given (cross-)correlations. Note that the noise auto-correlations L_{ii} are always determined by the concentration of the predator species A_i and its respective prey A_{i+1} , and the scale is set by the associated predation rate λ_i . Thus, the noise directly associated with a given species is solely determined by its role as predator.

Appendix A.3. Strongly asymmetric RPS model: mapping to the LV system

In order to investigate the asymmetric ‘‘corner’’ limit of the RPS system, we re-define the interaction rates as $\lambda_1 = \lambda/x$, $\lambda_2 = \lambda$ and $\lambda_3 = \kappa\lambda$. The dimensionless variable x varies in the interval $(0, 1]$ and describes the asymmetry of the rates, while the equally dimensionless parameter κ is of order unity and describes the difference between the predation rates of species A_2 and A_3 . We are interested in the limit $x \rightarrow 0$ in which the predation reactions between species A_1 and A_2 dominate. The concentrations at the coexistence fixed point become

$$(\Omega_1, \Omega_2, \Omega_3) = \rho(x, \kappa x, 1 - [1 + \kappa]x) + \mathcal{O}(x^2) . \quad (\text{A.15})$$

Hence, the densities of species A_1 and A_2 become small as $x \rightarrow 0$, while species A_3 makes up most of the overall species abundance. This is the ‘‘corner’’ limit in which RPS can be approximated by a two-species Lotka–Volterra system, with the third, most abundant species serving as a mean-field like reservoir to feed the first species, and to provide

the effective spontaneous death reaction for the second species, as explained above [51]. Species A_1 thus effectively turns into prey, while A_2 becomes the sole predator species. The noise correlation matrix L in this corner case reads

$$\begin{aligned} L_{11} &= \frac{\lambda}{x} a_1 a_2, & L_{12} &= -\frac{\lambda}{2x} a_1 a_2, & L_{13} &\approx -\frac{\kappa\lambda}{2} a_1 \rho, \\ L_{22} &\approx \lambda a_2 \rho, & L_{23} &\approx -\frac{\lambda}{2} a_2 \rho, & L_{33} &= \kappa\lambda a_1 \rho. \end{aligned}$$

The noise strength of species A_1 , as well as the noise cross-correlations between species A_1 and A_2 , are inversely proportional to the large rate scaling factor x , indicating that fluctuations of species A_1 and A_2 (the LV predator and prey, respectively) become strong in the limit $x \rightarrow 0$. Indeed, writing the resulting effective SPDEs in the limit of large λ_1 and assuming a homogeneous and stationary distribution of species A_3 yields

$$\partial_t a_1 \approx D_1 \nabla^2 a_1 + \lambda_1 a_1 a_2 - \rho \left(1 - \frac{\lambda_2 + \lambda_3}{\lambda_1} \right) \lambda_3 a_1 + \zeta_1, \quad (\text{A.16})$$

$$\partial_t a_2 \approx D_2 \nabla^2 a_2 + \rho \left(1 - \frac{\lambda_2 + \lambda_3}{\lambda_1} \right) \lambda_2 a_2 - \lambda_1 a_1 a_2 + \zeta_2, \quad (\text{A.17})$$

with the noise correlations

$$\langle \zeta_1(\vec{x}, t) \zeta_1(\vec{x}', t') \rangle = 2\lambda_1 a_1 a_2 \delta(\vec{x} - \vec{x}') \delta(t - t'), \quad (\text{A.18})$$

$$\langle \zeta_1(\vec{x}, t) \zeta_2(\vec{x}', t') \rangle = -\lambda_1 a_1 a_2 \delta(\vec{x} - \vec{x}') \delta(t - t'), \quad (\text{A.19})$$

$$\langle \zeta_2(\vec{x}, t) \zeta_2(\vec{x}', t') \rangle = 2\lambda_2 \rho \left(1 - \frac{\lambda_2 + \lambda_3}{\lambda_1} \right) a_2 \delta(\vec{x} - \vec{x}') \delta(t - t'). \quad (\text{A.20})$$

This set of Langevin equations precisely matches those derived directly for the LV model [34].

Appendix A.4. Fluctuation corrections

In order to gain more insight into the role of fluctuations in the RPS system, we study the non-linear vertices arising from the Doi–Peliti action (A.7). To this end, we first need to diagonalize the action by transforming to appropriate field combinations. We then list the resulting vertices that capture fluctuation corrections beyond the Gaussian mean-field approximation.

To start, we transform the fields to describe the fluctuations around the fixed-point species concentrations. To this end we employ the linear transformation

$$a_i(\vec{x}, t) = \Omega_i + c_i(\vec{x}, t), \quad \tilde{a}_i(\vec{x}, t) = \tilde{c}_i(\vec{x}, t), \quad (\text{A.21})$$

here ignoring higher-order shifts of the steady-state coexistence concentrations induced by stochastic fluctuations (i.e., the counter-terms or additive renormalizations in Ref. [34]). The action for these new fluctuating fields becomes

$$\mathcal{A} = \int dt d^d x \left[\sum_{i=1,2,3} \tilde{c}_i (\partial_t - D_i \nabla^2) c_i + \bar{\mathcal{A}} \right], \quad (\text{A.22})$$

Two-point (noise) sources \succ	
$\tilde{\phi}_\pm^2$	$+\frac{\rho\lambda_2}{(\lambda_1+\lambda_3)^2}\left(\rho\frac{\lambda_1^2(\lambda_2-\lambda_3)-\lambda_3^2(\lambda_1-\lambda_2)}{\lambda_1+\lambda_2+\lambda_3}\pm i\omega_0[\lambda_1-\lambda_3]\right)$
$\tilde{\phi}_+\tilde{\phi}_-$	$-\frac{2\rho^2\lambda_2}{\lambda_1+\lambda_3}\frac{\lambda_1\lambda_2+\lambda_1\lambda_3+\lambda_2\lambda_3}{\lambda_1+\lambda_2+\lambda_3}$
Merging three-point vertices $\leftarrow\leftarrow$	
$\tilde{\phi}_\pm\phi_\pm\psi$	$\pm 2i\frac{\omega_0}{\rho\lambda_2}\frac{(\lambda_1+\lambda_2+\lambda_3)^2}{\lambda_1+\lambda_3}$
$\tilde{\phi}_\pm\phi_\pm^2$	$+\left(\frac{\lambda_1+\lambda_2+\lambda_3}{\lambda_1+\lambda_3}\right)^2\left([\lambda_1-\lambda_3]\pm i\frac{\omega_0}{\rho\lambda_2}[\lambda_1-2\lambda_2+\lambda_3]\right)$
$\tilde{\phi}_\pm\phi_\mp^2$	$-\left(\frac{\lambda_1+\lambda_2+\lambda_3}{\lambda_1+\lambda_3}\right)^2\left([\lambda_1-\lambda_3]\pm i\frac{\omega_0}{\rho\lambda_2}[\lambda_1+2\lambda_2+\lambda_3]\right)$
Splitting three-point vertices $\searrow\leftarrow$	
$\psi\tilde{\phi}_\pm^2$	$\frac{2}{(\lambda_1+\lambda_3)^2}\left(\rho[\lambda_1^2(\lambda_2-\lambda_3)+\lambda_3^2(\lambda_2-\lambda_1)]\pm i\omega_0[\lambda_1-\lambda_3][\lambda_1+\lambda_2+\lambda_3]\right)$
$\psi\tilde{\phi}_+\tilde{\phi}_-$	$-\frac{4\rho}{\lambda_1+\lambda_3}(\lambda_1\lambda_2+\lambda_1\lambda_3+\lambda_2\lambda_3)$
$\phi_\pm\tilde{\psi}\tilde{\phi}_\pm$	$\pm 2i\omega_0\frac{\lambda_1+\lambda_2+\lambda_3}{\lambda_1+\lambda_3}$
$\phi_\pm\tilde{\phi}_\pm^2$	$\frac{\rho}{(\lambda_1+\lambda_3)^2}\left(\lambda_1\lambda_2[\lambda_1-\lambda_2]-\lambda_1\lambda_3[\lambda_1+\lambda_3]+2\lambda_2\lambda_3^2\pm\frac{\lambda_2\rho}{i\omega_0}[\lambda_2(\lambda_1^2-\lambda_3^2)+\lambda_1\lambda_3(\lambda_2+\lambda_3-2\lambda_1)]\right)$
$\phi_\pm\tilde{\phi}_\mp^2$	$-\frac{\rho}{(\lambda_1+\lambda_3)^3}\left(\lambda_1^2\lambda_2[\lambda_1+3\lambda_2-\lambda_3]+\lambda_1\lambda_3[\lambda_1\lambda_2]^2+2(\lambda_1^2+\lambda_2^2)\lambda_3^2+\lambda_1\lambda_3^3\pm\frac{\lambda_2\rho}{i\omega_0}[-\lambda_1^3\lambda_2+\lambda_1\lambda_3^3+\lambda_2\lambda_3^3+\lambda_1^2\lambda_3(2\lambda_2+\lambda_3)]\right)$
$\phi_\pm\tilde{\phi}_+\tilde{\phi}_-$	$\frac{2\rho}{(\lambda_1+\lambda_3)^2}\left(2\lambda_1\lambda_2^2+[\lambda_2^2-\lambda_1^2]\lambda_3-[\lambda_1+\lambda_2]\lambda_3^2\mp\frac{\lambda_2\rho}{i\omega_0}[\lambda_1^2(\lambda_2+\lambda_3)-\lambda_2\lambda_3^2-\lambda_1\lambda_2\lambda_3]\right)$

Table A1. Coefficients of the vertices in the action after the transformation to fluctuating fields.

with the reduced part

$$\begin{aligned} \bar{\mathcal{A}} = \frac{-1}{\bar{\lambda}^2} & \left[\lambda_1(\tilde{c}_1+1)(\tilde{c}_1-\tilde{c}_2)(\bar{\lambda}c_1+\lambda_2'\rho)(\bar{\lambda}c_2+\lambda_3\rho) \right. \\ & + \lambda_2'(\tilde{c}_2+1)(\tilde{c}_2-\tilde{c}_3)(\bar{\lambda}c_2+\lambda_3\rho)(\bar{\lambda}c_3+\lambda_1\rho) \\ & \left. + \lambda_3(\tilde{c}_3+1)(\tilde{c}_3-\tilde{c}_1)(\bar{\lambda}c_3+\lambda_1\rho)(\bar{\lambda}c_1+\lambda_2\rho) \right], \end{aligned} \quad (\text{A.23})$$

and $\bar{\lambda} = \lambda_1 + \lambda_2 + \lambda_3$. The harmonic part of this action can be cast in a bilinear matrix form $\bar{s}_h = \sum_{ij} \tilde{c}_j A_{ij} c_i$ with the mass matrix

$$A = \frac{\rho}{\bar{\lambda}} \begin{pmatrix} 0 & -\lambda_1\lambda_2 & \lambda_2\lambda_3 \\ \lambda_1\lambda_3 & 0 & -\lambda_2\lambda_3 \\ -\lambda_1\lambda_3 & \lambda_1\lambda_2 & 0 \end{pmatrix} = -A_s, \quad (\text{A.24})$$

where A_s is the stability matrix of the system at mean-field level. We note that it reduces to the stability matrix (4) in the symmetric limit $\lambda_1 = \lambda_2 = \lambda_3 = \lambda$.

Our goal is to find a transformation that diagonalizes the mass matrix A , and thus the harmonic part of the action (A.7), if we set all diffusivities equal, $D_i = D$. The matrix A is asymmetric, hence we make use of its orthogonal left and right eigenvectors $\vec{u}_i A = e_i \vec{u}_i$ and $A \vec{v}_i = e_i \vec{v}_i$, respectively. The resulting eigenvector matrices

$Q = (\vec{u}_1, \vec{u}_2, \vec{u}_3)$ and $P = (\vec{v}_1, \vec{v}_2, \vec{v}_3)$ read

$$Q = \begin{pmatrix} 1 & 1 & 1 \\ 1 & -\frac{\lambda_2(\lambda_1+\lambda_2)}{\lambda_2\lambda_3+i\Lambda} & -\frac{\lambda_2(\lambda_1+\lambda_2)}{\lambda_2\lambda_3-i\Lambda} \\ 1 & -\frac{\lambda_2(\lambda_2+\lambda_3)}{\lambda_1\lambda_2-i\Lambda} & -\frac{\lambda_2(\lambda_2+\lambda_3)}{\lambda_1\lambda_2+i\Lambda} \end{pmatrix}, \quad (\text{A.25})$$

where $\Lambda = \sqrt{\lambda_1\lambda_2\lambda_3(\lambda_1 + \lambda_2 + \lambda_3)}$, and

$$P = \begin{pmatrix} 1 & 1 & 1 \\ \frac{\lambda_3}{\lambda_2} & -\frac{\lambda_3(\lambda_1+\lambda_2)}{\lambda_2\lambda_3-i\Lambda} & -\frac{\lambda_3(\lambda_1+\lambda_2)}{\lambda_2\lambda_3+i\Lambda} \\ \frac{\lambda_1}{\lambda_2} & -\frac{\lambda_1(\lambda_2+\lambda_3)}{\lambda_1\lambda_2-i\Lambda} & -\frac{\lambda_1(\lambda_2+\lambda_3)}{\lambda_1\lambda_2+i\Lambda} \end{pmatrix}. \quad (\text{A.26})$$

The right and left eigenvector matrices then transform the mass matrix to the diagonal form $Q^T A P (Q^T P)^{-1} = \text{diag}(e_i)$. Defining new fields $\tilde{\phi}_i$ and ϕ_i according to the transformation $\tilde{c}_i = \sum_j Q_{ji}^T \tilde{\phi}_j$ and $c_i = \sum_j P_{ij} \phi_j$, we arrive at||

$$\begin{aligned} \tilde{c}_1 &= \tilde{\psi} + \tilde{\phi}_+ + \tilde{\phi}_-, \\ \tilde{c}_{2/3} &= \tilde{\psi} - \frac{\lambda_2}{\lambda_1 + \lambda_3} (\tilde{\phi}_+ + \tilde{\phi}_-) \pm \frac{i\Lambda/\lambda_{3/1}}{\lambda_1 + \lambda_3} (\tilde{\phi}_+ - \tilde{\phi}_-), \end{aligned} \quad (\text{A.27})$$

$$\begin{aligned} c_1 &= \psi + \phi_+ + \phi_-, \\ c_{2/3} &= \frac{\lambda_{3/1}}{\lambda_2} \psi - \frac{\lambda_{3/1}}{\lambda_1 + \lambda_3} (\phi_+ + \phi_-) \mp \frac{i\Lambda/\lambda_2}{\lambda_1 + \lambda_3} (\phi_+ - \phi_-). \end{aligned} \quad (\text{A.28})$$

It is already obvious from this structure that the fields $\tilde{\psi}$ and ψ describe the fluctuation of the total population, while the other fields are oscillatory in nature. Employing these transformations, one arrives at the diagonalized harmonic action

$$\begin{aligned} \mathcal{A}_0 &= \int dt \int d^d x (\lambda_1 + \lambda_2 + \lambda_3) \left[\frac{1}{\lambda_2} \tilde{\psi} (\partial_t - D\nabla^2) \psi \right. \\ &\quad \left. + \frac{1}{\lambda_1 + \lambda_3} \tilde{\phi}_+ (\partial_t - D\nabla^2 + i\omega_0) \phi_+ + \frac{1}{\lambda_1 + \lambda_3} \tilde{\phi}_- (\partial_t - D\nabla^2 - i\omega_0) \phi_- \right]. \end{aligned} \quad (\text{A.29})$$

The field $\psi = \lambda_2(c_1 + c_2 + c_3)/(\lambda_1 + \lambda_2 + \lambda_3)$ is massless, encodes no reactions, and is purely diffusive, as it represents the total local concentration of all three species. The corresponding harmonic propagator is given in Fourier space by

$$\langle \tilde{\psi}(\vec{q}, \omega) \psi(\vec{q}', \omega') \rangle = \frac{\lambda_2}{\lambda_1 + \lambda_2 + \lambda_3} \frac{(2\pi)^{d+1} \delta(\vec{q} + \vec{q}') \delta(\omega + \omega')}{-i\omega + Dq^2}, \quad (\text{A.30})$$

while the oscillating field propagators display poles at finite eigenfrequencies $\mp\omega_0$, similar to the LV case [34]. The action transformed to the new fields becomes quite cumbersome to write out in full, hence we merely provide the coefficients of the possible field combinations in the vertices in Table A1. Note that we omit the coefficients of any four-point vertices as these do not contribute to one-loop order corrections.

|| Note that we have employed a different diagonalization convention in this appendix as compared to the main text. This difference is reflected in the constant factors in the propagators.

Appendix B. Detailed calculations for the ML model

Here we provide intermediate steps for the one-loop calculation of the ML model. The renormalized frequencies are

$$\begin{aligned} \gamma_r \pm i\nu_r = & \gamma_0 \pm i\nu_0 + (\sigma + \kappa) \left[M_1^{(\pm)} \int_k \frac{1}{k^2 + \frac{\gamma_0}{D}} + M_2^{(\pm)} \int_k \frac{1}{k^2 + \frac{\gamma_0 \mp i\nu_0}{D}} \right. \\ & \left. + M_3^{(\pm)} \int_k \frac{1}{k^2 + \frac{\mu + \gamma_0 \pm i\nu_0}{2D}} + M_4^{(\pm)} \int_k \frac{1}{(k^2 + \frac{\gamma_0 \mp i\nu_0}{D})^2} + M_5^{(\pm)} \int_k \frac{1}{(k^2 + \frac{\mu + \gamma_0 \pm i\nu_0}{2D})^2} \right], \end{aligned} \quad (\text{B.1})$$

with the coefficients $M_i^{(\pm)} = \text{Re}M_i \pm \text{Im}M_i$, where

$$\begin{aligned} \text{Re}M_1 = & \frac{\gamma_0}{\sqrt{3}D\mu^2\nu_0 [(\gamma_0 - \mu)^2 + \nu_0^2]^2} \left[\gamma_0^2\mu(\gamma_0 - \mu)^4 - \nu_0^4(4\gamma_0^3 - 19\gamma_0^2\mu + 2\gamma_0\mu^2 + 8\mu^3) \right. \\ & \left. - \nu_0^2(\gamma_0 - \mu)^2(2\gamma_0^3 - 5\gamma_0^2\mu + 2\gamma_0\mu^2 + 3\mu^3) - \nu_0^6(2\gamma_0 + 5\mu) \right], \\ \text{Im}M_1 = & \frac{1}{\sqrt{3}D\mu^2 [(\gamma_0 - \mu)^2 + \nu_0^2]^2} \left[-\gamma_0^2\mu(\gamma_0 - \mu)^4 - \nu_0^4(4\gamma_0^3 - 17\gamma_0^2\mu + 2\gamma_0\mu^2 + 2\mu^3) \right. \\ & \left. - \nu_0^2(2\gamma_0^5 - \gamma_0^4\mu + 6\gamma_0^3\mu^2 - 8\gamma_0^2\mu^3 + \mu^5) - \nu_0^6(2\gamma_0 + \mu) \right], \\ \text{Re}M_2 = & -\frac{\gamma_0^2(\sqrt{3}\gamma_0 + \nu_0)}{3D\mu\nu_0}, \quad \text{Im}M_2 = \frac{\gamma_0(\sqrt{3}\gamma_0 + \nu_0)}{3D\mu}, \\ \text{Re}M_3 = & -\frac{\gamma_0}{3D\mu [(\gamma_0 - \mu)^2 + \nu_0^2]^2} \left[2\sqrt{3}\nu_0^3(6\gamma_0^2 - \gamma_0\mu - 3\mu^2) + \nu_0^4(\gamma_0 + \mu) \right. \\ & \left. + 2\nu_0^2(\gamma_0 - \mu)^2(\gamma_0 + \mu) - 2\sqrt{3}\mu\nu_0(\gamma_0 - \mu)^2(\gamma_0 + \mu) + (\gamma_0 - \mu)^4(\gamma_0 + \mu) - 4\sqrt{3}\nu_0^5 \right], \\ \text{Im}M_3 = & \frac{\gamma_0\nu_0}{3D\mu [(\gamma_0 - \mu)^2 + \nu_0^2]^2} \left[2\sqrt{3}\nu_0(2\gamma_0^3 + \gamma_0^2\mu - 4\gamma_0\mu^2 + \mu^3) + 2\sqrt{3}\nu_0^3(\mu - 6\gamma_0) \right. \\ & \left. - 2\nu_0^2(\gamma_0 - \mu)^2 - (\gamma_0 - \mu)^4 - \nu_0^4 \right], \\ \text{Re}M_4 = & -\frac{(\gamma_0 + \sqrt{3}\nu_0)(\gamma_0^2 + \nu_0^2)}{6D^2\mu}, \quad \text{Im}M_4 = \frac{\gamma_0(\gamma_0^2 + \nu_0^2)}{\sqrt{3}D^2\mu}, \\ \text{Re}M_5 = & -\frac{\gamma_0}{6D^2\mu [(\gamma_0 - \mu)^2 + \nu_0^2]} \left[\gamma_0^4 - \gamma_0^3(\mu - 2\sqrt{3}\nu_0) - \gamma_0^2\mu^2 \right. \\ & \left. + \gamma_0(\mu - 2\sqrt{3}\nu_0)(\mu^2 + 3\nu_0^2) - \nu_0^2(\mu^2 + \nu_0^2) \right], \\ \text{Im}M_5 = & -\frac{\gamma_0\nu_0}{6D^2\mu [(\gamma_0 - \mu)^2 + \nu_0^2]} \left[2\gamma_0^3 - 3\gamma_0^2(\mu - 2\sqrt{3}\nu_0) + 2\gamma_0\nu_0^2 \right. \\ & \left. + (\mu - 2\sqrt{3}\nu_0)(\mu^2 + \nu_0^2) \right]. \end{aligned} \quad (\text{B.2})$$

The renormalized diffusivity is

$$\begin{aligned}
D_r^\pm = & D - (\kappa + \sigma) \left[\frac{(\gamma_0 - \sqrt{3}\nu_0)}{3dD\mu} (\gamma_0 \mp i\nu_0) \int_k \frac{k^2}{\left(k^2 + \frac{\gamma_0 \mp i\nu_0}{D}\right)^3} \right. \\
& - \frac{\gamma_0}{3dD\mu} (\gamma_0 + \mu \pm i\nu_0) \int_k \frac{k^2}{\left(k^2 + \frac{\mu + \gamma_0 \pm i\nu_0}{2D}\right)^3} \\
& \mp i \frac{2\sqrt{3}\gamma_0}{3dD^2\mu} (\gamma_0^2 + \nu_0^2) (\gamma_0 \mp i\nu_0) \int_k \frac{1}{\left(k^2 + \frac{\gamma_0 \mp i\nu_0}{D}\right)^3} \\
& + \frac{2\sqrt{3}\gamma_0}{3dD\mu\nu_0} (\gamma_0^2 + \nu_0^2) \int_k \frac{1}{\left(k^2 + \frac{\gamma_0 \mp i\nu_0}{D}\right)^2} \pm i \frac{2\sqrt{3}\gamma_0}{3d\mu\nu_0^2} (\gamma_0^2 + \nu_0^2) \int_k \frac{1}{k^2 + \frac{\gamma_0 \mp i\nu_0}{D}} \\
& - \frac{\sqrt{3}\gamma_0\nu_0(\gamma_0 + \mu \pm i\nu_0)^2}{3dD^2\mu(-\gamma_0 + \mu \pm i\nu_0)} \int_k \frac{1}{\left(k^2 + \frac{\mu + \gamma_0 \pm i\nu_0}{2D}\right)^3} \\
& - \frac{4\sqrt{3}\gamma_0^2\nu_0(\gamma_0 + \mu \pm i\nu_0)}{3dD\mu(-\gamma_0 + \mu \pm i\nu_0)^2} \int_k \frac{1}{\left(k^2 + \frac{\mu + \gamma_0 \pm i\nu_0}{2D}\right)^2} \\
& - \frac{8\sqrt{3}\gamma_0^2\nu_0(\gamma_0 + \mu \pm i\nu_0)}{3d\mu(-\gamma_0 + \mu \pm i\nu_0)^3} \int_k \frac{1}{k^2 + \frac{\mu + \gamma_0 \pm i\nu_0}{2D}} \\
& \left. + \frac{2\gamma}{\sqrt{3}d\mu\nu_0^2} \left[\frac{4\gamma\nu_0^3(\gamma + \mu + i\nu_0)}{(-\gamma + \mu + i\nu_0)^3} - i(\gamma^2 + \nu_0^2) \right] \int_k \frac{1}{k^2 + \frac{\gamma_0}{D}} \right], \tag{B.3}
\end{aligned}$$

and can be further simplified to

$$\begin{aligned}
D_r^\pm = & D + \frac{\kappa + \sigma}{d} \left[P_3^{(\pm)} \int_k \frac{1}{\left(k^2 + \frac{\gamma_0 \mp i\nu_0}{D}\right)^3} + P_2^{(\pm)} \int_k \frac{1}{\left(k^2 + \frac{\gamma_0 \mp i\nu_0}{D}\right)^2} + P_1^{(\pm)} \int_k \frac{1}{k^2 + \frac{\gamma_0 \mp i\nu_0}{D}} \right. \\
& + Q_3^{(\pm)} \int_k \frac{1}{\left(k^2 + \frac{\mu + \gamma_0 \pm i\nu_0}{2D}\right)^3} + Q_2^{(\pm)} \int_k \frac{1}{\left(k^2 + \frac{\mu + \gamma_0 \pm i\nu_0}{2D}\right)^2} + Q_1^{(\pm)} \int_k \frac{1}{k^2 + \frac{\mu + \gamma_0 \pm i\nu_0}{2D}} \\
& \left. - \left(P_1^{(\pm)} + Q_1^{(\pm)} \right) \int_k \frac{1}{k^2 + \frac{\gamma_0}{D}} \right], \tag{B.4}
\end{aligned}$$

where $P_i^{(\pm)} = \text{Re}P_i \pm i\text{Im}P_i$ and $Q_i^{(\pm)} = \text{Re}Q_i \pm i\text{Im}Q_i$, with

$$\begin{aligned}
\text{Re}P_1 &= 0, & \text{Im}P_1 &= \frac{2\gamma_0(\gamma_0^2 + \nu_0^2)}{\sqrt{3}\mu\nu_0^2}, \\
\text{Re}P_2 &= \frac{\gamma_0(2\sqrt{3}\gamma_0^2 - \gamma_0\nu_0 + 3\sqrt{3}\nu_0^2)}{3D\mu\nu_0}, & \text{Im}P_2 &= \frac{\nu_0(\gamma_0 - \sqrt{3}\nu_0)}{3D\mu}, \\
\text{Re}P_3 &= \frac{(\gamma_0^3 - 3\sqrt{3}\gamma_0^2\nu_0 - \gamma_0\nu_0^2 - \sqrt{3}\nu_0^3)}{3D^2\mu}, & \text{Im}P_3 &= -\frac{2\gamma_0^2(\sqrt{3}\gamma_0 + \nu_0)}{3D^2\mu}, \\
\text{Re}Q_1 &= \frac{8\gamma_0^2\nu_0[6\gamma_0\nu_0^2(\mu - \gamma_0) + (\gamma_0 - \mu)^3(\gamma_0 + \mu) + \nu_0^4]}{\sqrt{3}\mu[(\gamma_0 - \mu)^2 + \nu_0^2]^3}, \\
\text{Im}Q_1 &= \frac{16\gamma_0^2\nu_0^2(2\gamma_0^3 - 3\gamma_0^2\mu - 2\gamma_0\nu_0^2 + \mu^3 + \mu\nu_0^2)}{\sqrt{3}\mu[(\gamma_0 - \mu)^2 + \nu_0^2]^3}, \\
\text{Re}Q_2 &= -\frac{\gamma_0}{3D\mu[(\gamma_0 - \mu)^2 + \nu_0^2]^2} \left[\gamma_0^5 + \gamma_0^4(4\sqrt{3}\nu_0 - 3\mu) \right. \\
&\quad \left. + 2\gamma_0^3(\mu^2 - 2\sqrt{3}\mu\nu_0 + \nu_0^2) + 2\gamma_0^2(\mu^3 - 2\sqrt{3}\mu^2\nu_0 - \mu\nu_0^2 - 6\sqrt{3}\nu_0^3) \right. \\
&\quad \left. - \gamma_0(3\mu^2 - 4\sqrt{3}\mu\nu_0 - \nu_0^2)(\mu^2 + \nu_0^2) + \mu(\mu^2 + \nu_0^2)^2 \right], \\
\text{Im}Q_2 &= \frac{\gamma_0\nu_0[-2\nu_0^2(\gamma_0 - \mu)^2 - 4\sqrt{3}\gamma_0\nu_0(3\gamma_0 + \mu)(\gamma_0 - \mu) - (\gamma_0 - \mu)^4 + 4\sqrt{3}\gamma_0\nu_0^3 - \nu_0^4]}{3D\mu[(\gamma_0 - \mu)^2 + \nu_0^2]^2}, \\
\text{Re}Q_3 &= \frac{\gamma_0}{6D^2\mu[(\gamma_0 - \mu)^2 + \nu_0^2]} \left[\gamma_0^4 + 2\sqrt{3}\gamma_0^3\nu_0 - 2\gamma_0^2\mu(\mu - \sqrt{3}\nu_0) \right. \\
&\quad \left. - 2\gamma_0\nu_0(\sqrt{3}\mu^2 - 2\mu\nu_0 + 3\sqrt{3}\nu_0^2) + (\mu^2 - 2\sqrt{3}\mu\nu_0 - \nu_0^2)(\mu^2 + \nu_0^2) \right], \\
\text{Im}Q_3 &= \frac{\gamma_0\nu_0[\nu_0^2(\gamma_0 + \mu) + \sqrt{3}\nu_0(3\gamma_0 - \mu)(\gamma_0 + \mu) + (\gamma_0 - \mu)^2(\gamma_0 + \mu) - \sqrt{3}\nu_0^3]}{3D^2\mu[(\gamma_0 - \mu)^2 + \nu_0^2]}.
\end{aligned} \tag{B.5}$$

Appendix C. Renormalized variables in the ML model at physically accessible dimensions

Finally, we list the expressions of the renormalized variables at physically accessible dimensions $d = 1, 2$, and 3 .

Appendix C.1. $d = 1$:

For the ψ_o mode, the renormalized parameters read

$$\begin{aligned}
\mu_r &= \mu \left[1 - \frac{5(\sigma + \kappa)}{24D} \sqrt{\frac{D}{\mu}} - \frac{\sigma + \kappa}{D} \sqrt{\frac{D}{\gamma_0}} \left(\frac{1}{12} + \frac{\gamma_0}{3\mu} + \frac{\sqrt{3}\nu_0}{16\mu} + \frac{\sqrt{3}\nu_0}{16\gamma_0} + \frac{\sqrt{3}\nu_0\gamma_0}{6\mu^2} \right) \right], \\
D_r^0 &= D - \frac{\sigma + \kappa}{48} \sqrt{\frac{D}{\mu}} - \frac{\sigma + \kappa}{24} \sqrt{\frac{D}{\gamma_0}} \left(\frac{\gamma_0}{\mu} - \frac{\sqrt{3}\nu_0}{2\mu} + \frac{\sqrt{3}\nu_0}{2\gamma_0} \right).
\end{aligned} \tag{C.1}$$

For the ψ_{\pm} modes, when $\gamma_0 \geq 0$, the renormalized parameters are

$$\begin{aligned}
\gamma_r = & \gamma_0 + (\sigma + \kappa) \sqrt{\frac{D}{\nu_0}} \left[\frac{1}{2} \text{Re} M_1 \sqrt{\frac{\nu_0}{\gamma_0}} + \frac{1}{2} \left(1 + \frac{\gamma_0^2}{\nu_0^2} \right)^{-1/4} \left(\text{Re} M_2 \cos \frac{\theta}{2} - \text{Im} M_2 \sin \frac{\theta}{2} \right) \right. \\
& + \frac{\sqrt{2}}{2} \left(1 + \frac{(\gamma_0 + \mu)^2}{\nu_0^2} \right)^{-1/4} \left(\text{Re} M_3 \cos \frac{\eta}{2} + \text{Im} M_3 \sin \frac{\eta}{2} \right) \\
& + \frac{D}{4\nu_0} \left(1 + \frac{\gamma_0^2}{\nu_0^2} \right)^{-3/4} \left(\text{Re} M_4 \cos \frac{3\theta}{2} - \text{Im} M_4 \sin \frac{3\theta}{2} \right) \\
& \left. + \frac{\sqrt{2}D}{2\nu_0} \left(1 + \frac{(\mu + \gamma_0)^2}{\nu_0^2} \right)^{-3/4} \left(\text{Re} M_5 \cos \frac{3\eta}{2} + \text{Im} M_5 \sin \frac{3\eta}{2} \right) \right], \\
\nu_r = & \nu_0 + (\sigma + \kappa) \sqrt{\frac{D}{\nu_0}} \left[\frac{1}{2} \text{Im} M_1 \sqrt{\frac{\nu_0}{\gamma_0}} + \frac{1}{2} \left(1 + \frac{\gamma_0^2}{\nu_0^2} \right)^{-1/4} \left(\text{Re} M_2 \sin \frac{\theta}{2} + \text{Im} M_2 \cos \frac{\theta}{2} \right) \right. \\
& + \frac{\sqrt{2}}{2} \left(1 + \frac{(\gamma_0 + \mu)^2}{\nu_0^2} \right)^{-1/4} \left(-\text{Re} M_3 \sin \frac{\eta}{2} + \text{Im} M_3 \cos \frac{\eta}{2} \right) \\
& + \frac{D}{4\nu_0} \left(1 + \frac{\gamma_0^2}{\nu_0^2} \right)^{-3/4} \left(\text{Re} M_4 \sin \frac{3\theta}{2} + \text{Im} M_4 \cos \frac{3\theta}{2} \right) \\
& \left. + \frac{\sqrt{2}D}{2\nu_0} \left(1 + \frac{(\mu + \gamma_0)^2}{\nu_0^2} \right)^{-3/4} \left(-\text{Re} M_5 \sin \frac{3\eta}{2} + \text{Im} M_5 \cos \frac{3\eta}{2} \right) \right]; \tag{C.2}
\end{aligned}$$

yet if $\gamma_0 < 0$, the first term in both parameters changes:

$$\begin{aligned}
\gamma_r = & \gamma_0 + (\sigma + \kappa) \sqrt{\frac{D}{\nu_0}} \left[-\frac{1}{2} \text{Im} M_1 \sqrt{\frac{\nu_0}{|\gamma_0|}} + \frac{1}{2} \left(1 + \frac{\gamma_0^2}{\nu_0^2} \right)^{-1/4} \left(\text{Re} M_2 \cos \frac{\theta}{2} - \text{Im} M_2 \sin \frac{\theta}{2} \right) \right. \\
& + \frac{\sqrt{2}}{2} \left(1 + \frac{(\gamma_0 + \mu)^2}{\nu_0^2} \right)^{-1/4} \left(\text{Re} M_3 \cos \frac{\eta}{2} + \text{Im} M_3 \sin \frac{\eta}{2} \right) \\
& + \frac{D}{4\nu_0} \left(1 + \frac{\gamma_0^2}{\nu_0^2} \right)^{-3/4} \left(\text{Re} M_4 \cos \frac{3\theta}{2} - \text{Im} M_4 \sin \frac{3\theta}{2} \right) \\
& \left. + \frac{\sqrt{2}D}{2\nu_0} \left(1 + \frac{(\mu + \gamma_0)^2}{\nu_0^2} \right)^{-3/4} \left(\text{Re} M_5 \cos \frac{3\eta}{2} + \text{Im} M_5 \sin \frac{3\eta}{2} \right) \right], \\
\nu_r = & \nu_0 + (\sigma + \kappa) \sqrt{\frac{D}{\nu_0}} \left[\frac{1}{2} \text{Re} M_1 \sqrt{\frac{\nu_0}{|\gamma_0|}} + \frac{1}{2} \left(1 + \frac{\gamma_0^2}{\nu_0^2} \right)^{-1/4} \left(\text{Re} M_2 \sin \frac{\theta}{2} + \text{Im} M_2 \cos \frac{\theta}{2} \right) \right. \\
& + \frac{\sqrt{2}}{2} \left(1 + \frac{(\gamma_0 + \mu)^2}{\nu_0^2} \right)^{-1/4} \left(-\text{Re} M_3 \sin \frac{\eta}{2} + \text{Im} M_3 \cos \frac{\eta}{2} \right) \\
& + \frac{D}{4\nu_0} \left(1 + \frac{\gamma_0^2}{\nu_0^2} \right)^{-3/4} \left(\text{Re} M_4 \sin \frac{3\theta}{2} + \text{Im} M_4 \cos \frac{3\theta}{2} \right) \\
& \left. + \frac{\sqrt{2}D}{2\nu_0} \left(1 + \frac{(\mu + \gamma_0)^2}{\nu_0^2} \right)^{-3/4} \left(-\text{Re} M_5 \sin \frac{3\eta}{2} + \text{Im} M_5 \cos \frac{3\eta}{2} \right) \right]. \tag{C.3}
\end{aligned}$$

The renormalized diffusivity is not affected by the sign of γ_0 ,

$$\begin{aligned}
\text{Re}D_r = D + (\kappa + \sigma) & \sqrt{\frac{D}{\nu_0}} \left[-\frac{1}{2} \left(1 + \frac{\gamma_0^2}{\nu_0^2}\right)^{-1/4} \text{Im}P_1 \sin \frac{\theta}{2} - \frac{1}{2} \text{Re}Q_1 \sqrt{\frac{\nu_0}{\gamma_0}} \right. \\
& + \frac{D}{4\nu_0} \left(1 + \frac{\gamma_0^2}{\nu_0^2}\right)^{-3/4} \left(\text{Re}P_2 \cos \frac{3\theta}{2} - \text{Im}P_2 \sin \frac{3\theta}{2} \right) \\
& + \frac{3D^2}{16\nu_0^2} \left(1 + \frac{\gamma_0^2}{\nu_0^2}\right)^{-5/4} \left(\text{Re}P_3 \cos \frac{5\theta}{2} - \text{Im}P_3 \sin \frac{5\theta}{2} \right) \\
& + \frac{\sqrt{2}}{2} \left(1 + \frac{(\mu + \gamma_0)^2}{\nu_0^2}\right)^{-1/4} \left(\text{Re}Q_1 \cos \frac{\eta}{2} + \text{Im}Q_1 \sin \frac{\eta}{2} \right) \\
& + \frac{\sqrt{2}D}{2\nu_0} \left(1 + \frac{(\mu + \gamma_0)^2}{\nu_0^2}\right)^{-3/4} \left(\text{Re}Q_2 \cos \frac{3\eta}{2} + \text{Im}Q_2 \sin \frac{3\eta}{2} \right) \\
& \left. + \frac{3\sqrt{2}D^2}{4\nu_0^2} \left(1 + \frac{(\mu + \gamma_0)^2}{\nu_0^2}\right)^{-5/4} \left(\text{Re}Q_3 \cos \frac{5\eta}{2} + \text{Im}Q_3 \sin \frac{5\eta}{2} \right) \right]. \tag{C.4}
\end{aligned}$$

Appendix C.2. $d = 2$:

For the ψ_o mode, the renormalized parameters read

$$\begin{aligned}
\mu_r = \mu & \left[1 - \frac{\sigma + \kappa \gamma_0}{6D\pi} \frac{1}{\mu} \ln \frac{D\Lambda^2}{\gamma_0} - \frac{\sigma + \kappa}{12D\pi} \ln \frac{D\Lambda^2}{\mu} - \frac{\sigma + \kappa}{24D\pi} \right. \\
& \left. - \frac{\sigma + \kappa}{12D\pi} \left(1 + \frac{\sqrt{3}\nu_0}{2\mu} + \frac{\sqrt{3}\nu_0}{2\gamma_0} + \frac{2\sqrt{3}\nu_0\gamma_0}{\mu^2} \right) \right], \tag{C.5} \\
D_r^o = D & - \frac{\sigma + \kappa}{48\pi} - \frac{\sigma + \kappa}{24\pi} \left(\frac{\gamma_0}{\mu} - \frac{2\sqrt{3}\nu_0}{3\mu} + \frac{\sqrt{3}\nu_0}{3\gamma_0} \right).
\end{aligned}$$

For the ψ_{\pm} modes, the renormalized parameters are

$$\begin{aligned}
\gamma_r = & \gamma_0 + \frac{\sigma + \kappa}{2\pi} \left[\frac{\text{Re}M_1}{2} \ln \frac{D\Lambda^2}{\gamma_0} + (\text{Re}M_2 + \text{Re}M_3) \ln \Lambda - \theta \text{Im}M_2 + \eta \text{Im}M_3 \right. \\
& - \frac{1}{4} \left[\text{Re}M_2 \ln \frac{\gamma_0^2 + \nu_0^2}{D^2} + \text{Re}M_3 \ln \frac{(\mu + \gamma_0)^2 + \nu_0^2}{4D^2} \right] \\
& + \frac{D}{2\nu_0} \left(1 + \frac{\gamma_0^2}{\nu_0^2} \right)^{-1/2} (\text{Re}M_4 \cos \theta - \text{Im}M_4 \sin \theta) \\
& \left. + \frac{D}{\nu_0} \left(1 + \frac{(\mu + \gamma_0)^2}{\nu_0^2} \right)^{-1/2} (\text{Re}M_5 \cos \eta + \text{Im}M_5 \sin \eta) \right], \\
\nu_r = & \nu_0 + \frac{\sigma + \kappa}{2\pi} \left[\frac{\text{Im}M_1}{2} \ln \frac{D\Lambda^2}{\gamma_0} + (\text{Im}M_2 + \text{Im}M_3) \ln \Lambda + \theta \text{Re}M_2 - \eta \text{Re}M_3 \right. \\
& - \frac{1}{4} \left[\text{Im}M_2 \ln \frac{\gamma_0^2 + \nu_0^2}{D^2} + \text{Im}M_3 \ln \frac{(\mu + \gamma_0)^2 + \nu_0^2}{4D^2} \right] \\
& + \frac{D}{2\nu_0} \left(1 + \frac{\gamma_0^2}{\nu_0^2} \right)^{-1/2} (\text{Re}M_4 \sin \theta + \text{Im}M_4 \cos \theta) \\
& \left. + \frac{D}{\nu_0} \left(1 + \frac{(\mu + \gamma_0)^2}{\nu_0^2} \right)^{-1/2} (-\text{Re}M_5 \sin \eta + \text{Im}M_5 \cos \eta) \right],
\end{aligned} \tag{C.6}$$

and the renormalized diffusivity is

$$\begin{aligned}
\text{Re}D_r = & D + \frac{\kappa + \sigma}{2\pi} \left[-\frac{\text{Re}Q_1}{8} \ln \frac{\nu_0^2 + (\mu + \gamma_0)^2}{4\gamma_0^2} + \frac{1}{4} (\eta \text{Im}Q_1 - \theta \text{Im}P_1) \right. \\
& + \frac{D}{4\nu_0} \left(1 + \frac{\gamma_0^2}{\nu_0^2} \right)^{-1/2} (\text{Re}P_2 \cos \theta - \text{Im}P_2 \sin \theta) \\
& + \frac{D^2}{8\nu_0^2} \left(1 + \frac{\gamma_0^2}{\nu_0^2} \right)^{-1} (\text{Re}P_3 \cos 2\theta - \text{Im}P_3 \sin 2\theta) \\
& + \frac{D}{2\nu_0} \left(1 + \frac{(\mu + \gamma_0)^2}{\nu_0^2} \right)^{-1/2} (\text{Re}Q_2 \cos \eta + \text{Im}Q_2 \sin \eta) \\
& \left. + \frac{D^2}{2\nu_0^2} \left(1 + \frac{(\mu + \gamma_0)^2}{\nu_0^2} \right)^{-1} (\text{Re}Q_3 \cos 2\eta + \text{Im}Q_3 \sin 2\eta) \right].
\end{aligned} \tag{C.7}$$

Appendix C.3. $d = 3$:

For the ψ_o mode, the renormalized parameters read

$$\begin{aligned}
\mu_r = & \mu \left[1 + \frac{\sigma + \kappa}{16D\pi} \sqrt{\frac{\mu}{D}} + \frac{\sigma + \kappa}{6D\pi} \sqrt{\frac{\gamma_0}{D}} \left(-\frac{1}{4} + \frac{\gamma_0}{\mu} - \frac{\sqrt{3}\nu_0}{16\mu} - \frac{\sqrt{3}\nu_0}{16\gamma_0} - \frac{\sqrt{3}\nu_0\gamma_0}{2\mu^2} \right) \right], \\
D_r^o = & D - \frac{\sigma + \kappa}{96\pi} \sqrt{\frac{\mu}{D}} - \frac{\sigma + \kappa}{48\pi} \sqrt{\frac{\gamma_0}{D}} \left(\frac{\sqrt{3}\nu_0}{6\gamma_0} + \frac{\gamma_0}{\mu} - \frac{5\sqrt{3}\nu_0}{6\mu} \right).
\end{aligned} \tag{C.8}$$

For the ψ_{\pm} modes, if $\bar{\gamma}_0 \geq 0$, the renormalized parameters are

$$\begin{aligned}
\gamma_r = & \gamma_0 + \frac{\sigma + \kappa}{4\pi} \sqrt{\frac{\nu_0}{D}} \left[-\operatorname{Re}M_1 \sqrt{\frac{\gamma_0}{\nu_0}} - \left(1 + \frac{\gamma_0^2}{\nu_0^2}\right)^{1/4} \left(\operatorname{Re}M_2 \cos \frac{\theta}{2} + \operatorname{Im}M_2 \sin \frac{\theta}{2}\right) \right. \\
& - \frac{\sqrt{2}}{2} \left(1 + \frac{(\mu + \gamma_0)^2}{\nu_0^2}\right)^{1/4} \left(\operatorname{Re}M_3 \cos \frac{\eta}{2} - \operatorname{Im}M_3 \sin \frac{\eta}{2}\right) \\
& + \frac{D}{2\nu_0} \left(1 + \frac{\gamma_0^2}{\nu_0^2}\right)^{-1/4} \left(\operatorname{Re}M_4 \cos \frac{\theta}{2} - \operatorname{Im}M_4 \sin \frac{\theta}{2}\right) \\
& \left. + \frac{\sqrt{2}D}{2\nu_0} \left(1 + \frac{(\mu + \gamma_0)^2}{\nu_0^2}\right)^{-1/4} \left(\operatorname{Re}M_5 \cos \frac{\eta}{2} + \operatorname{Im}M_5 \sin \frac{\eta}{2}\right) \right], \\
\nu_r = & \nu_0 + \frac{\sigma + \kappa}{4\pi} \sqrt{\frac{\nu_0}{D}} \left[-\operatorname{Im}M_1 \sqrt{\frac{\gamma_0}{\nu_0}} - \left(1 + \frac{\gamma_0^2}{\nu_0^2}\right)^{1/4} \left(-\operatorname{Re}M_2 \sin \frac{\theta}{2} + \operatorname{Im}M_2 \cos \frac{\theta}{2}\right) \right. \\
& - \frac{\sqrt{2}}{2} \left(1 + \frac{(\mu + \gamma_0)^2}{\nu_0^2}\right)^{1/4} \left(\operatorname{Re}M_3 \sin \frac{\eta}{2} + \operatorname{Im}M_3 \cos \frac{\eta}{2}\right) \\
& + \frac{D}{2\nu_0} \left(1 + \frac{\gamma_0^2}{\nu_0^2}\right)^{-1/4} \left(\operatorname{Re}M_4 \sin \frac{\theta}{2} + \operatorname{Im}M_4 \cos \frac{\theta}{2}\right) \\
& \left. + \frac{\sqrt{2}D}{2\nu_0} \left(1 + \frac{(\mu + \gamma_0)^2}{\nu_0^2}\right)^{-1/4} \left(-\operatorname{Re}M_5 \sin \frac{\eta}{2} + \operatorname{Im}M_5 \cos \frac{\eta}{2}\right) \right].
\end{aligned} \tag{C.9}$$

When $\gamma_0 < 0$ and the system is rendered unstable, the renormalized parameters become

$$\begin{aligned}
\mu_r = & \left[1 + \frac{\sigma + \kappa}{16D\pi} \sqrt{\frac{\mu}{D}} + \frac{\sigma + \kappa}{6D\pi} \sqrt{\frac{\gamma_0}{D}} \left(-\frac{1}{4} + \frac{\gamma_0}{\mu} - \frac{\sqrt{3}\nu_0}{16\mu} - \frac{\sqrt{3}\nu_0}{16\gamma_0} - \frac{\sqrt{3}\nu_0\gamma_0}{2\mu^2} \right) \right], \\
D_r^{\circ} = & D - \frac{\sigma + \kappa}{96\pi} \sqrt{\frac{\mu}{D}} - \frac{\sigma + \kappa}{48\pi} \sqrt{\frac{\gamma_0}{D}} \left(\frac{\sqrt{3}\nu_0}{6\gamma_0} + \frac{\gamma_0}{\mu} - \frac{5\sqrt{3}\nu_0}{6\mu} \right).
\end{aligned} \tag{C.10}$$

For the ψ_{\pm} modes, for $\bar{\gamma}_0 \geq 0$, the renormalized parameters are

$$\begin{aligned}
\gamma_r = & \gamma_0 + \frac{\sigma + \kappa}{4\pi} \sqrt{\frac{\nu_0}{D}} \left[-\text{Im}M_1 \sqrt{\frac{|\gamma_0|}{\nu_0}} - \left(1 + \frac{\gamma_0^2}{\nu_0^2}\right)^{1/4} \left(\text{Re}M_2 \cos \frac{\theta}{2} + \text{Im}M_2 \sin \frac{\theta}{2}\right) \right. \\
& - \frac{\sqrt{2}}{2} \left(1 + \frac{(\mu + \gamma_0)^2}{\nu_0^2}\right)^{1/4} \left(\text{Re}M_3 \cos \frac{\eta}{2} - \text{Im}M_3 \sin \frac{\eta}{2}\right) \\
& + \frac{D}{2\nu_0} \left(1 + \frac{\gamma_0^2}{\nu_0^2}\right)^{-1/4} \left(\text{Re}M_4 \cos \frac{\theta}{2} - \text{Im}M_4 \sin \frac{\theta}{2}\right) \\
& \left. + \frac{\sqrt{2}D}{2\nu_0} \left(1 + \frac{(\mu + \gamma_0)^2}{\nu_0^2}\right)^{-1/4} \left(\text{Re}M_5 \cos \frac{\eta}{2} + \text{Im}M_5 \sin \frac{\eta}{2}\right) \right], \\
\nu_r = & \nu_0 + \frac{\sigma + \kappa}{4\pi} \sqrt{\frac{\nu_0}{D}} \left[\text{Re}M_1 \sqrt{\frac{|\gamma_0|}{\nu_0}} - \left(1 + \frac{\gamma_0^2}{\nu_0^2}\right)^{1/4} \left(-\text{Re}M_2 \sin \frac{\theta}{2} + \text{Im}M_2 \cos \frac{\theta}{2}\right) \right. \\
& - \frac{\sqrt{2}}{2} \left(1 + \frac{(\mu + \gamma_0)^2}{\nu_0^2}\right)^{1/4} \left(\text{Re}M_3 \sin \frac{\eta}{2} + \text{Im}M_3 \cos \frac{\eta}{2}\right) \\
& + \frac{D}{2\nu_0} \left(1 + \frac{\gamma_0^2}{\nu_0^2}\right)^{-1/4} \left(\text{Re}M_4 \sin \frac{\theta}{2} + \text{Im}M_4 \cos \frac{\theta}{2}\right) \\
& \left. + \frac{\sqrt{2}D}{2\nu_0} \left(1 + \frac{(\mu + \gamma_0)^2}{\nu_0^2}\right)^{-1/4} \left(-\text{Re}M_5 \sin \frac{\eta}{2} + \text{Im}M_5 \cos \frac{\eta}{2}\right) \right].
\end{aligned} \tag{C.11}$$

The renormalized diffusivity is not affected by the sign of γ_0 ,

$$\begin{aligned}
\text{Re}D_r = & D + \frac{\kappa + \sigma}{3\pi} \sqrt{\frac{\nu_0}{D}} \left[-\frac{1}{4} \left(1 + \frac{\gamma_0^2}{\nu_0^2}\right)^{1/4} \text{Im}P_1 \sin \frac{\theta}{2} + \frac{1}{4} \text{Re}Q_1 \sqrt{\frac{\gamma_0}{\nu_0}} \right. \\
& + \frac{D}{8\nu_0} \left(1 + \frac{\gamma_0^2}{\nu_0^2}\right)^{-1/4} \left(\text{Re}P_2 \cos \frac{\theta}{2} - \text{Im}P_2 \sin \frac{\theta}{2}\right) \\
& + \frac{D^2}{32\nu_0^2} \left(1 + \frac{\gamma_0^2}{\nu_0^2}\right)^{-3/4} \left(\text{Re}P_3 \cos \frac{3\theta}{2} - \text{Im}P_3 \sin \frac{3\theta}{2}\right) \\
& - \frac{\sqrt{2}}{8} \left(1 + \frac{(\mu + \gamma_0)^2}{\nu_0^2}\right)^{1/4} \left(\text{Re}Q_1 \cos \frac{\eta}{2} - \text{Im}Q_1 \sin \frac{\eta}{2}\right) \\
& + \frac{\sqrt{2}D}{8\nu_0} \left(1 + \frac{(\mu + \gamma_0)^2}{\nu_0^2}\right)^{-1/4} \left(\text{Re}Q_2 \cos \frac{\eta}{2} + \text{Im}Q_2 \sin \frac{\eta}{2}\right) \\
& \left. + \frac{\sqrt{2}D^2}{16\nu_0^2} \left(1 + \frac{(\mu + \gamma_0)^2}{\nu_0^2}\right)^{-3/4} \left(\text{Re}Q_3 \cos \frac{3\eta}{2} + \text{Im}Q_3 \sin \frac{3\eta}{2}\right) \right].
\end{aligned} \tag{C.12}$$

References

- [1] R. M. May. *Stability and Complexity in Model Ecosystems*. Princeton University Press, 1973.
- [2] J. Maynard-Smith. *Models in Ecology*. Cambridge University Press, 1974.
- [3] J. D. Murray. *Mathematical Biology: I. An Introduction*. Springer, 2002.

- [4] J. Hofbauer and K. Sigmund. *Evolutionary Games and Population Dynamics*. Cambridge University Press, 1998.
- [5] A. J. Lotka. Undamped oscillations derived from the law of mass action. *Journal of the American Chemical Society*, 42:1595, 1920.
- [6] V. Volterra. *Variazioni e fluttuazioni del numero d'individui in specie animali conviventi*. Società anonima tipografica "Leonardo da Vinci", 1926.
- [7] J. M. Smith. *Evolution and the Theory of Games*. Cambridge University Press, 1982.
- [8] T. Reichenbach, M. Mobilia, and E. Frey. Mobility promotes and jeopardizes biodiversity in rock–paper–scissors games. *Nature*, 448:1046, 2007.
- [9] T. Reichenbach, M. Mobilia, and E. Frey. Self-organization of mobile populations in cyclic competition. *Journal of Theoretical Biology*, 254:368, 2008.
- [10] Q. He, M. Mobilia, and U. C. Täuber. Spatial rock-paper-scissors models with inhomogeneous reaction rates. *Physical Review E*, 82:051909, 2010.
- [11] R. M. May and W. J. Leonard. Nonlinear aspects of competition between three species. *SIAM Journal on Applied Mathematics*, 29:243, 1975.
- [12] E. Frey. Evolutionary game theory: Theoretical concepts and applications to microbial communities. *Physica A: Statistical Mechanics and its Applications*, 389:4265, 2010.
- [13] Q. He, M. Mobilia, and U. C. Täuber. Coexistence in the two-dimensional May–Leonard model with random rates. *The European Physical Journal B*, 82:97, 2011.
- [14] S. Rulands, A. Zielinski, and E. Frey. Global attractors and extinction dynamics of cyclically competing species. *Physical Review E*, 87:052710, 2013.
- [15] S. Rulands, T. Reichenbach, and E. Frey. Threefold way to extinction in populations of cyclically competing species. *Journal of Statistical Mechanics: Theory and Experiment*, 2011:L01003, 2011.
- [16] S. R. Serrao and U. C. Täuber. A stochastic analysis of the spatially extended May–Leonard model. *Journal of Physics A: Mathematical and Theoretical*, 50:404005, 2017.
- [17] C. Elton and M. Nicholson. The ten-year cycle in numbers of the lynx in Canada. *The Journal of Animal Ecology*, page 215, 1942.
- [18] S. Utida. Cyclic fluctuations of population density intrinsic to the host-parasite system. *Ecology*, 38:442, 1957.
- [19] B. E. McLaren and R. O. Peterson. Wolves, moose, and tree rings on isle royale. *Science*, 266:1555, 1994.
- [20] B. Kerr, M. A. Riley, M. W. Feldman, and B. J. M. Bohannan. Local dispersal promotes biodiversity in a real-life game of rock–paper–scissors. *Nature*, 418:171, 2002.

- [21] B. C. Kirkup and M. A. Riley. Antibiotic-mediated antagonism leads to a bacterial game of rock–paper–scissors in vivo. *Nature*, 428:412, 2004.
- [22] L. K. Mühlbauer, M. Schulze, W. S. Harpole, and A. T. Clark. gauseR: Simple methods for fitting Lotka–Volterra models describing Gause’s “Struggle for Existence”. *Ecology and Evolution*, 10:13275, 2020.
- [23] R. Durrett. Stochastic spatial models. *SIAM review*, 41:677, 1999.
- [24] A. Provata, G. Nicolis, and F. Baras. Oscillatory dynamics in low-dimensional supports: a lattice Lotka–Volterra model. *The Journal of Chemical Physics*, 110:8361, 1999.
- [25] M. Mobilia, I. T. Georgiev, and U. C. Täuber. Phase transitions and spatio-temporal fluctuations in stochastic lattice Lotka–Volterra models. *Journal of Statistical Physics*, 128:447, 2007.
- [26] M. J. Washenberger, M. Mobilia, and U. C. Täuber. Influence of local carrying capacity restrictions on stochastic predator–prey models. *Journal of Physics: Condensed Matter*, 19:065139, 2007.
- [27] A. J. McKane and T. J. Newman. Predator–prey cycles from resonant amplification of demographic stochasticity. *Physical Review Letters*, 94:218102, 2005.
- [28] T. Butler and D. Reynolds. Predator–prey quasicycles from a path-integral formalism. *Physical Review E*, 79:032901, 2009.
- [29] U. C. Täuber. Stochastic population oscillations in spatial predator–prey models. *Journal of Physics: Conference Series*, 319:012019, 2011.
- [30] U. Dobramysl, M. Mobilia, M. Pleimling, and U. C. Täuber. Stochastic population dynamics in spatially extended predator–prey systems. *Journal of Physics A: Mathematical and Theoretical*, 51:063001, 2018.
- [31] U. Dobramysl and U. C. Täuber. Spatial variability enhances species fitness in stochastic predator–prey interactions. *Physical Review Letters*, 101:258102, 2008.
- [32] U. Dobramysl and U. C. Täuber. Environmental versus demographic variability in two-species predator–prey models. *Physical Review Letters*, 110:048105, 2013.
- [33] A. Dobrinevski and E. Frey. Extinction in neutrally stable stochastic Lotka–Volterra models. *Physical Review E*, 85:051903, 2012.
- [34] U. C. Täuber. Population oscillations in spatial stochastic Lotka–Volterra models: a field-theoretic perturbational analysis. *Journal of Physics A: Mathematical and Theoretical*, 45:405002, 2012.
- [35] U. C. Täuber. *Critical Dynamics: A Field Theory Approach to Equilibrium and Non-Equilibrium Scaling Behavior*. Cambridge University Press, 2014.
- [36] U. C. Täuber, M. Howard, and B. P. Vollmayr-Lee. Applications of field-theoretic renormalization group methods to reaction–diffusion problems. *Journal of Physics A: Mathematical and General*, 38:R79, 2005.

- [37] H. K. Janssen. On a Lagrangean for classical field dynamics and renormalization group calculations of dynamical critical properties. *Zeitschrift für Physik B Condensed Matter*, 23:377, 1976.
- [38] C. De Dominicis. Technics of field renormalization and dynamics of critical phenomena. In *J. Phys.(Paris), Colloq*, page C1, 1976.
- [39] J. Zinn-Justin. *Quantum Field Theory and Critical Phenomena*, volume 171. Oxford University Press, 2021.
- [40] M. C. Cross and P. C. Hohenberg. Pattern formation outside of equilibrium. *Reviews of Modern Physics*, 65:851, 1993.
- [41] P C Hohenberg and M C Cross. An introduction to pattern formation in nonequilibrium systems. In *Fluctuations and Stochastic Phenomena in Condensed Matter*, page 55. Springer, 1987.
- [42] M. Doi. Second quantization representation for classical many-particle system. *Journal of Physics A: Mathematical and General*, 9:1465, 1976.
- [43] M. Doi. Stochastic theory of diffusion-controlled reaction. *Journal of Physics A: Mathematical and General*, 9:1479, 1976.
- [44] P. Grassberger and M. Scheunert. Fock-space methods for identical classical objects. *Fortschritte der Physik*, 28:547, 1980.
- [45] L. Peliti. Path integral approach to birth-death processes on a lattice. *Journal de Physique*, 46:1469, 1985.
- [46] D. C. Mattis and M. L. Glasser. The uses of quantum field theory in diffusion-limited reactions. *Reviews of Modern Physics*, 70:979, 1998.
- [47] J. Cardy, G. Falkovich, K. Gawędzki, S. Nazarenko, and O.V. Zaboronski. *Non-equilibrium Statistical Mechanics and Turbulence*. London Mathematical Society Lecture Note Series. Cambridge University Press, 2008.
- [48] T. Butler and N. Goldenfeld. Robust ecological pattern formation induced by demographic noise. *Physical Review E*, 80:030902, 2009.
- [49] T. Butler and N. Goldenfeld. Fluctuation-driven turing patterns. *Physical Review E*, 84:011112, 2011.
- [50] R. Bausch, H. K. Janssen, and H. Wagner. Renormalized field theory of critical dynamics. *Zeitschrift für Physik B Condensed Matter*, 24:113, 1976.
- [51] Q. He, U. C. Täuber, and R. K. P. Zia. On the relationship between cyclic and hierarchical three-species predator-prey systems and the two-species Lotka-Volterra model. *The European Physical Journal B*, 85:1, 2012.